EFFICIENT LIGHT TRANSMISSION THROUGH SINGLE SUB-WAVELENGTH HOLES

Dissertation

zur

Erlangung des Doktorgrades (Dr. rer. nat.)

der

Mathematisch-Naturwissenschaftlichen Fakultät

der

Rheinischen Friedrich-Wilhelms-Universität Bonn

vorgelegt von

Felix Kalkum

aus Heidelberg

Bonn 2009

Angefertigt mit Genehmigung der Mathematisch Naturwissenschaftlichen
Fakultät der Rheinischen Friedrich-Wilhelm-Universität Bonn

Erstgutachter: Prof. Dr. Karsten Buse
Zweitgutachter: Prof. Dr. Manfred Fiebig

Tag der Promotion: 27.11.2009
Erscheinungsjahr: 2009

Contents

Chapter 1

Introduction

Photonic crystals [1], optical metamaterials [2,3], near-field microscopy [4], and plasmonics [5, 6] are recent innovations in modern optics. These and more ideas are subsumed by the term "nanophotonics".

To compensate for the small interaction volume – and thus a small interaction efficiency of each part of a nanostructure – a high contrast of the dielectric constant is needed. Looking for materials with extreme values, metal appears on the top of the list. Only a few ten nanometers of metal film can suffice to make it virtually opaque at optical wavelengths. Furthermore, nowadays the technology to fabricate metal structures with sizes far below the wavelength of visible light is readily available.

However, there is a tough side of nanophotonics: Light opposes the idea of being squeezed into structures far below its wavelength. For example: The thinner a plasmonic waveguide gets, the higher is the damping [6]. As the tip of a near-field microscope gets smaller and smaller, the transmission through the sub-wavelength hole on its cone end is drastically reduced [7]. In practice, limitations like these obviate the widespread use of nanophotonics in real-life applications. And the issue naturally arises of how to address these structures most efficiently.

The scope of the work presented herein are two approaches to efficiently address and enhance the throughput of the most simple nanostructure: A sub-wavelength hole in a metal film. Recent interest in transmission properties of sub-wavelength holes arises from a report that this transmission can be drastically enhanced by regular hole patterns [8]. The question of how this enhancement works has been subject to vivid discussion. Nowadays, the common interpretation is that nanostructures in metal films generate surface waves, which may constructively interfere at

the hole. By using circular concentric corrugations around a single hole, an enhancement by one order of magnitude can be achieved [9]. In contrast, the two approaches presented herein rely on the constructive interference of the impinging waves for enhanced light transmission.

When light impinges on a metal film with a sub-wavelength hole, most of it is reflected, only a small portion is absorbed and a very tiny fraction is transmitted through the hole. One approach pursued in this work is to place a partially transmitting mirror before the metal film. The metal film and the mirror thus form a cavity, which can augment the transmittance through the system. This is the so-called Fabry-Pérot effect. In practice, the enhancement is limited by misalignment, surface imperfections and absorption. These factors also reduce the finesse of the system. Thus, the enhancement and the finesse of the resonator are measured for different transmission coefficients of the input mirror. The questions under investigation are, which enhancement can be reached in reality for an optimal input transmission coefficient, and how this enhancement can be compared with the previously mentioned method of structuring the surface surrounding the hole.

The larger part of this work is devoted to a method of efficiently directing light to sub-wavelength holes in a metal film: Holographic phase conjugation. The light transmits through the hole, serves as a signal wave S and interferes with a plane reference wave R. An iron-doped lithium niobate crystal translates the interference pattern into a hologram. This hologram is read-out with the phase-conjugated reference wave R^*, which is the plane wave counter-propagating to the reference beam R. According to the holographic principle, the phase-conjugated signal wave S^* is reconstructed. Since S is essentially a spherical wave emerging from the sub-wavelength hole, S^* is a wave being focused onto the hole.

The aim of these investigations concerning holographic phase conjugation through a sub-wavelength hole is to understand which factors determine the power ratio of the light being deflected onto the sub-wavelength hole versus the reference light impinging onto the crystal. This value is the so-called diffraction efficiency. Beyond looking for an increase of the transmission efficiency, we ask whether improvements can be achieved for two possible applications: Addressing sub-wavelength structures, which are distributed over a large area, and, after removing the metal film, an easy-to-fabricate device for focusing light near the diffraction limit.

Chapter 2

Sub-wavelength holes

Unlike its solution, stating the problem is simple: How much light is transmitted through a hole with a diameter smaller than the wavelength and how does the light diffract behind the hole? Consider the situation shown in Fig. 2.1: Monochromatic light with the electric field vector $\boldsymbol{A}_{\mathbf{in}}$ impinges perpendicularly onto an optically opaque material. In the material there is a small circular hole with a radius r_h smaller than the wavelength λ of the impinging light. A small amount of the impinging light is transmitted through the hole and is diffracted behind it. One might ask, what fraction of the power impinging onto the hole is transmitted through it. This is the so-called transmission efficiency T_h:

$$T_\mathrm{h} = \frac{P_\mathrm{t}}{I_\mathrm{in}\pi r_\mathrm{h}^2}, \tag{2.1}$$

where I_in is the intensity of the impinging light, and P_t is the total transmitted light power. Furthermore, we would like to know the field distribution $\boldsymbol{A}_{\mathbf{t}}$ of the light behind the hole.

Early answers to this question date back to the seventeenth century with huge progress in the twentieth century [10]. But still today, there is no satisfactory answer, which is generally agreed upon. While there is a huge amount of literature on this question with recent review articles [10, 11], it is not our aim to give a complete overview on this subject, but to brief on it with the goal to identify the knowledge which is useful for the work presented thereafter.

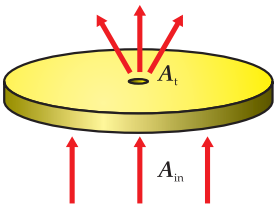

Figure 2.1: A light wave $\boldsymbol{A_{in}}$ impinges onto an opaque screen with a sub-wavelength hole. Part of the light is transmitted and diffracted in the space behind the screen.

2.1 Theory

A first approach to solve the question of light transmittance through a tiny hole is given by Kirchhoff's scalar diffraction theory [12]. This theory assumes the most simple boundary conditions for the problem: The light field is set to zero at the opaque screen and is set to the incoming wave A_{in} in the aperture. From this assumptions the scalar light field behind the hole can be computed. For holes large compared to the wavelength λ, the light is mainly propagating in the direction of the incident light and the power rapidly decreases for deviating directions. Thus, the transmitted light power is the power impinging on the hole and the transmission coefficient is $T_{\text{h}} = 1$.

Though Kirchhoff's theory gives very good results for large holes, it fails for very small ones. As the aperture gets smaller, the light diffracts more and more until it bends towards the opaque screen. The transmission efficiency is no longer one but decreases proportional to $T_{\text{h}} = (r_{\text{h}}/\lambda)^2$. Furthermore, the light wave becomes non-zero at the opaque screen in contradiction to the assumed boundary conditions. A second shortcoming of Kirchhoff's theory is that it is scalar, but as the hole gets smaller, a real vectorial description is needed.

In 1944 Bethe presented a solution for the problem [7]. He assumed that the opaque screen is infinitely thin and a perfect electrical conductor and that the diameter of the hole is much smaller than the wavelength of the incoming light: $r_{\text{h}} \ll \lambda$. Thus, he could assume that the fields are constant over the area of the hole. From this assumptions he derived a vectorial description of the problem. The transmission efficiency is found

to be:

$$T_{\mathrm{h}} = \frac{64}{27\pi^2} k^4 r_{\mathrm{h}}^4, \tag{2.2}$$

where $k = 2\pi/\lambda$ is the length of the wave vector of the light. Thus, the transmitted power falls off much more rapidly with the hole diameter than predicted by Kirchhoff's theory. Behind the hole, the diffracted light $\boldsymbol{A_t}$ is described by a magnetic dipole radiation, where the magnetic dipole is in the plane of the screen and perpendicular to the incident electric field vector.

One attempt to generalize Bethe's result is made by Roberts [13]. His calculations allow a finite thickness of the screen and any hole radius. The field in the hole is described by circular waveguide modes instead of Bethe's assumption of a constant field. This field is matched to the field of the incoming and transmitted light. In the theory not only propagating, but also evanescent modes are considered. Though there is no propagating mode for hole diameters smaller than the so-called cut-off radius $r_{\mathrm{h}} < 1.84/k$, for thin films a finite transmission is found due to the non-propagating modes. For thick films, the cut-off becomes more and more relevant until virtually no light is transmitted for a radius below the cut-off. For very large hole diameters, the transmission efficiency becomes $T_{\mathrm{h}} = 1$ in accordance to Kirchhoff's scalar theory. A calculation of the transmission efficiency for an infinitely thin screen is shown in Fig. 2.2. Roberts also compared the diffraction patterns to those calculated using the Kirchhoff theory for $kr_{\mathrm{h}} = 5$, $kr_{\mathrm{h}} = 10$, $kr_{\mathrm{h}} = 15$. Virtually no differences are found for an infinitely thin screen. However, some widening of the diffraction pattern in the direction parallel to the incident electrical field occurs for a screen with a thickness comparable or larger than the hole radius.

Up to now, a perfect electrical conductor with an infinite electric conductivity and no penetration of the field into the metal is assumed. In reality, especially at optical wavelengths, this assumption is not correct. Several percent of the light impinging onto a metal surface can be absorbed, and the electric fields might penetrate several tens of nanometers into the material [12]. This is expected to profoundly change the transmission characteristics of a sub-wavelength hole. First, since the light wave can penetrate into the metal, the effective radius of the hole becomes larger. Remembering the rapid decrease of the transmission efficiency with the hole radius in Eq. 2.2, a drastic change of the transmission is expected. Furthermore, the waveguide structure can be profoundly changed by the

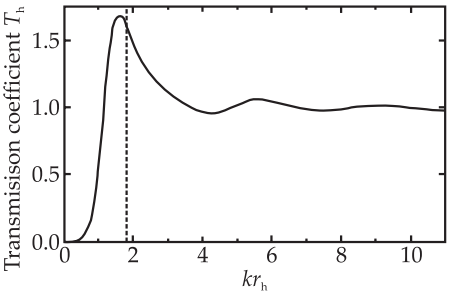

Figure 2.2: Transmission coefficient T_h for a circular hole with radius r_h in an infinitely thin perfect electrical conductor as predicted by [13]. The cut-off at $kr_h = 1.84$ is marked with a dashed line.

transfer from a perfect electrical conductor to a real metal [14–16]. Even anomalous modes might come into play, which correspond to imaginary solutions of the waveguide Eigenvalue problem and correspond to neither propagating nor evanescent waves [17].

2.2 Experiments

The enormous interest in the transmission through sub-wavelength apertures was triggered in 1998, by a report stating that the transmission efficiency is enhanced by three orders of magnitude for a regular pattern of sub-wavelength holes compared to Bethe's formula [8]. This report interprets the effect as caused by a resonant excitation of surface plasmon polaritons on the front and back side of the metal film [18]. These polaritons are surface waves originating from the coupling of an electromagnetic wave and the electron gas at the metal surface [19]. On a plane metal surface the surface plasmon and a freely propagating wave can not couple because of a mismatch of the dispersion relations. But regular gratings, like the structures in the experiments of Ebbesen et al., could provide the coupling [8].

The order of magnitude of the enhancement stated in the paper by Ebbesen et al. was called in question later [20]: If the transmitted power is related to experimental values of a single hole and not to Bethe's for-

mula, an enhancement factor of about seven is found, two orders of magnitudes less than claimed earlier. Furthermore, though the transmission is enhanced at some wavelengths, suppression below the single hole transmission is found at others, which is completely unexpected from the point of view of surface plasmon polariton excitation. Hence, a new model was proposed, called "composite diffracted evanescent wave model", where the role of surface plasmon polariton waves is neglected [20]. There, the observed transmission pattern is attributed to the interference of evanescent waves, originating from the sub-wavelength structures.

Further progress was made by studying arrays of sub-wavelength slits in contrast to circular holes. Since the problem reduces to one dimension, it simplifies. By numerical finite difference time domain simulations it is found that the observed transmission spectra are due to two effects: A Fabry-Pérot effect in the slit, since light is partially reflected at the entrance and exit of the slit, and interference of surface waves launched by the slits [21]. The latter effect is illustrated in Fig. 2.3. The nature of the surface waves still lacks of an adequate interpretation. Experimental [22, 23] and theoretical analysis [24–26] suggest that both, long-ranging surface plasmon polaritons and quickly fading evanescent waves, are launched by the sub-wavelength slit. The interference of these waves accounts for the observed enhancement and suppression of the transmission of the slit arrays. However, the details of these interferences are still poorly understood [11].

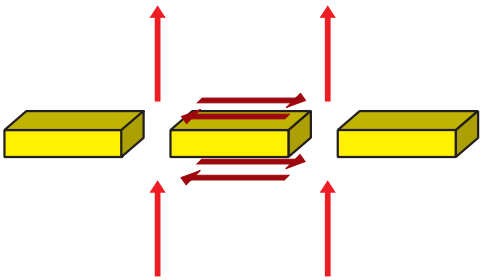

Figure 2.3: Interference of the impinging and transmitted light with surface waves launched by sub-wavelength slits enhances or suppresses light transmission through a regular array of slits.

Additionally, it was the interest in scanning near-field optical microscopes, which led to experimental investigations on the transmission characteristics of single circular holes in the optical range [27]. Latter reports tend to interpret the results in terms of the excitation and coupling of surface plasmons [28–30]. However, it is still unclear whether such an interpretation is adequate. Though there is agreement upon the idea that surface plasmon polaritons are probably launched at a sub-wavelength hole, their role is yet unknown. And even more important, up to now, no surface plasmon polariton interpretation seems to succeed in predicting the transmission characteristics of sub-wavelength holes. Furthermore, experiments to measure the transmission efficiency through a single hole seem to be extremely challenging, even more so, as the fabrication of the metal film and the hole have to be extremely well controlled for accurate measurements. Therefore, the question of how much light is transmitted through a tiny hole is still considered to be open [10, 11].

Although the transmission efficiency for a single sub-wavelength hole is not accurately described by theory, it can be enhanced, i.e., the transmission efficiency is increased by some means compared to the efficiency without those means. One such method is to surround the sub-wavelength hole with concentric periodic grooves [9, 31, 32]. Surface waves launched by the grooves can constructively interfere at the hole, increasing the light transmission. So, the light is effectively harvested from a much larger area then the hole but finally is collected there. An increase of the transmission efficiency by one order of magnitude is gained in this way.

2.3 Applications

Aside from their use in the tip of near-field scanning optical microscopes [4], sub-wavelength holes were used and proposed for a variety of applications [10]. These include an ultrafast photodetector, where the extremely small area behind a sub-wavelength hole is used as a detector area, but concentric grooves are employed to enhance the efficiency of the device [33]. An optically thick aluminum layer with sub-wavelength holes is applied as a cathode in an organic light emitting device, increasing the light output [34]. Sub-wavelength apertures can also be used for lithography below the diffraction limit [35–37].

Chapter 3

Fabry-Pérot enhancement

Now, we study a straightforward arrangement to enhance the transmitted power through a sub-wavelength hole: The metal film with a sub-wavelength hole is used as one mirror of a Fabry-Pérot interferometer. When light impinges on the metal film, the largest part of the light is reflected. Only a tiny fraction is transmitted through the hole. By placing a second mirror before the metal film, the reflected light gets further chances of being transmitted through the hole. This idea is illustrated in Fig. 3.1. For coherent light, if no losses occurred, 100 % of the light impinging onto the setup would be transmitted through the hole at resonance, despite the fact that the transmittance through the hole is so small. This is the Fabry-Pérot effect. In reality, the transmittance is limited by imperfections of the mirrors, non-optimal alignment, absorption in the metal film, and by diffraction. The question arises, whether in practice an enhancement can be gained and if so, whether it can compete with other methods to enhance the transmittance through sub-wavelength holes.

3.1 Background

We consider an ideal plane-parallel Fabry-Pérot interferometer: A monochromatic plane wave impinges onto a partially transmitting input mirror. Due to an output mirror, aligned parallel, the light wave bounces forth and back between the two mirrors. Then, the transmission versus the distance of the two mirrors can be described by a chain of Lorentz curves [38]. When the mirror distance is an integer multiple of half the wavelength, constructive interference occurs, and the transmitted fraction

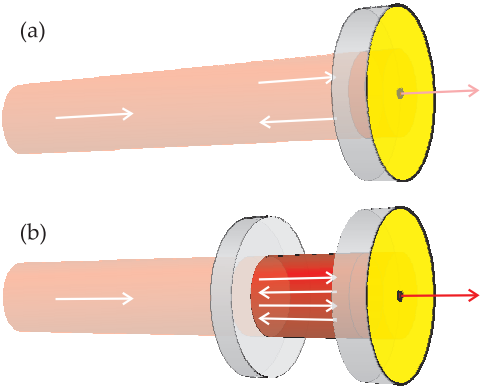

Figure 3.1: Scheme for Fabry-Pérot-enhanced transmission through a sub-wavelength hole. (a) When light hits a metal surface with a sub-wavelength hole, only a tiny amount is transmitted through the hole. The biggest part of the light is reflected. (b) By placing a dielectric mirror in front of the metal surface, the reflected light gets more chances of being transmitted through the hole. The intensity in front of the hole is enhanced and so is the transmitted light power.

of the incident power reaches a maximum:

$$T_{\max} = \frac{T_1 T_2}{(1-\sqrt{R})^2}. \tag{3.1}$$

Here $R = R_1 R_2$ is the reflection per round trip, R_1 and R_2 are the reflection coefficients of the input and output mirrors, and T_1 and T_2 are the transmission coefficients of the two surfaces. If no losses occur, the transmission can reach 100 %, even for extremely small transmission coefficients T_1 and T_2. All R and T values refer to the intensity and not to the field amplitude.

The reflective finesse of the interferometer, which describes the quality of the resonator without any imperfection and misalignment, is defined by:

$$F_{\mathrm{r}} = \frac{\pi R^{\frac{1}{4}}}{1-\sqrt{R}}, \tag{3.2}$$

and for large F the finesse is approximately the free spectral range λ_{F}, i.e., the distance of two transmission peaks, divided by the full width at half maximum of a transmission peak $\Delta\lambda$.

Now we assume that the second mirror is a substrate with an optically thick gold film with a sub-wavelength hole in it. Then, the transmission coefficient T_2 is determined by the transmission coefficient of the hole and the size of the hole compared with the size of the impinging wave. Thus, T_2 is negligibly small. Furthermore, since the hole is much smaller than the wavelength of the light, we do not expect that the mode structure of the light in the resonator is disturbed. Hence, in deriving the peak transmission $T_{\max}$ through the system with hole the same line of reasoning as for Eq. (3.1) can be applied. Since we want to know how much the transmission through the hole is enhanced by the presence of the dielectric input mirror, we define the enhancement E by:

$$E = \frac{T_{\max}}{T_2} = \frac{T_1}{(1-\sqrt{R})^2}. \tag{3.3}$$

This corresponds to our experimental procedure, where we divide the peak power of the transmitted light with input mirror by the power of the transmitted light without input mirror.

Without any losses, for $T_1 \ll 1$ and $T_2 \ll T_1$, thus if $R \approx 1 - T_1$, the enhancement is $E \approx 4/T_1$. Hence, E could reach giant values. Yet, in practice some losses occur. A dielectric mirror with negligible loss can be

used as input mirror. However, some absorption might be unavoidable for the thick metal film at the exit surface.

In practice, imperfections of the mirror surfaces, alignment errors, diffraction, and absorption decrease the effective finesse F_e and therefore the enhancement E. A way to account for these effects is to model the interferometer divided in several ideal interferometers with different mirror distances and finally to sum up the intensities of all interferometers [39]. Thus, the transmission function is convolved with a function describing the distribution of phase deviations.

Unfortunately, the function needed to account for the different mirror distances is not known in most practical situations. A reasonable assumption is that the phase deviation can be described by a Gauss curve. The convolution of a Lorentz curve, i.e., a peak of the transmission function, and the Gauss error curve results in a so-called Voigt profile. For the width and the height of the Voigt profile approximate closed-form expressions are available [40, 41]. We write these formula in terms of an effective finesse F_e corresponding to the combined profile, the original reflective finesse F_r, and a limiting finesse F_l, which is the maximal achievable finesse in the system [40]:

$$\frac{1}{F_e} = \frac{1}{2}\left[1.0692\frac{1}{F_r} + \sqrt{0.86639\frac{1}{F_r^2} + 4\frac{1}{F_l^2}}\right]. \tag{3.4}$$

The transmitted intensity changes by the factor [41]:

$$\frac{(\pi/2)(F_e/F_r)}{1.065 + 0.447(F_e/F_r) + 0.058(F_e/F_r)^2}. \tag{3.5}$$

In the literature it is usually assumed that it suffices to convolve the transmitted intensity with the function describing the phase deviations. However, convolving the amplitude instead of the intensity is supposed to serve as a better approximation. We numerically convolve the Fabry-Pérot transmittance function for the amplitude with a Gaussian error distribution and find that the peak height of the intensity is very well approximated by using the square of the factor in Eq. 3.5. Thus the enhancement becomes:

$$E = \frac{T_{max}}{T_2} = \frac{T_1}{(1-\sqrt{R})^2}\left(\frac{(\pi/2)(F_e/F_r)}{1.065 + 0.447(F_e/F_r) + 0.058(F_e/F_r)^2}\right)^2. \tag{3.6}$$

In practice, the uncoated surface of the substrate is inside the resonator and has a small non-zero reflectivity R_G. This is illustrated in Fig. 3.2. Because of this, the Fabry-Pérot interferometer actually consists of two coupled interferometers: The one formed by the first mirror and the uncoated surface of the substrate and the one formed by the uncoated substrate and the gold film. We approximate this model by considering the situation, where the dielectric mirror and the uncoated surface form an effective mirror. The enhancement is supposedly maximal for maximal reflectivity of the effective mirror. Thus, we use an effective reflectivity of the combined mirror:

$$R_1^{\text{eff}} = 1 - \frac{T_1 T_G}{1 + \sqrt{R_1 R_G}}. \tag{3.7}$$

The transmission is corrected correspondingly.

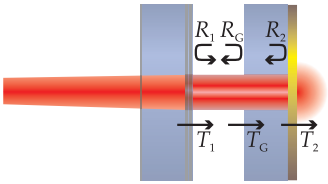

Figure 3.2: Scheme of the surfaces involved in a practical setup for Fabry-Pérot-enhanced transmission through a sub-wavelength hole. The transmission and reflection coefficients of the input mirror (T_1, R_1), of the uncoated substrate surface (T_G, R_G), and of the exit mirror (T_2, R_2) are assigned to their respective surfaces.

3.2 Methods

Figure 3.3 shows the experimental setup. A tunable external cavity fiber laser (1), with vacuum wavelengths $\lambda_0 = 1470$–$1583\,\text{nm}$ is used as a light source. The light is coupled out of the fiber (2). Two mirrors not shown in the figure are used to align the beam and to sent the light onto the dielectric mirror (3). The substrate (4) is coated on the output side with a gold film with sub-wavelength holes in it. The light being transmitted through the sub-wavelength holes is collected by a NA $= 0.65$ microscope objective (5) and imaged together with a lens (7) onto an InGaAs diode (8). The

aperture (6) which is used at the position of the objective's image has a diameter of 5 mm. This aperture ensures that neighboring pinholes in the surface do not contribute to the measured transmitted light.

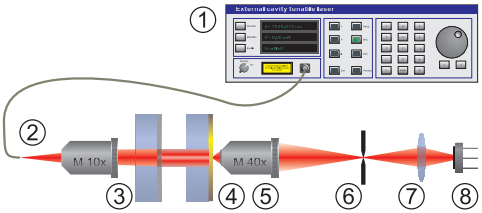

Figure 3.3: Experimental setup to measure the power transmitted through a sub-wavelength hole in a gold film. Enhancement by the Fabry-Pérot effect is used. The numbers are explained in the text.

Three different dielectric mirrors are used. They each are designed for certain reflection coefficients at one wavelength. For wavelengths deviating from their design values the reflection coefficients differ such that a wide range of reflection R_1 and transmission coefficients $T_1 = 1 - R_1$ can be used by exploiting the tuning capability of the infrared laser. The actual transmission coefficients are measured for each wavelength which is used for the enhancement measurements. The back sides of the dielectric mirrors are anti-reflection coated.

The fused-silica substrate (4) is specified for a flatness of $\lambda/20$ at $\lambda = 633$ nm and for a wedge angle smaller than 0.2 arcseconds. One surface of the substrate is coated with a (300 ± 30)-nm-thick gold film. The thickness is determined with an electron microscope. Experimentally, the reflectivity of the gold surface is found to be $R_2 = 0.980 \pm 0.005$. A focused ion beam is used to drill holes into the surface. Single holes as well as ensembles of ten sub-wavelength holes positioned arbitrarily in a 10-μm-wide region are made. The total light transmission through the ensembles is higher than for a single hole and thus increases the signal-to-noise ratio. A periodic arrangement is avoided, to circumvent interference effects as found by Ebbesen et al. [8]. Such an ensemble is shown in Fig. 3.4. To make this picture the focused ion beam is not only used for drilling the holes but also used for imaging. For the transmission measurements an ensemble with ten 600-nm holes is used.

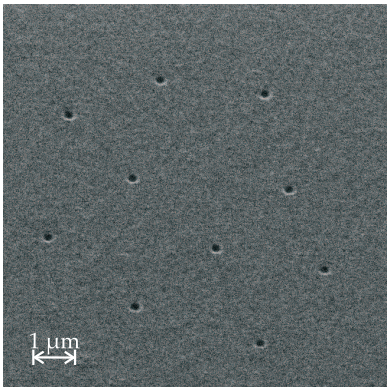

Figure 3.4: Focused-ion-beam picture of the gold surface with ten sub-wavelength holes. (Photo: A. Sehrbrock, Forschungszentrum caesar)

The distance between the first dielectric mirror (3) and the substrate (4) is about 6 mm. The fused silica substrate (4) has an index of refraction of $n = 1.45$ at the wavelength $\lambda_0 = 1550\,\text{nm}$ and a thickness of 5 mm. Thus, the optical path length of one round trip in the resonator is $d_\text{o} = 2 \times (6\,\text{mm} + 1.45 \times 5\,\text{mm}) = 26.5\,\text{mm}$ and, hence, the free spectral range, i.e., the distance of two transmission peaks, is $\nu_\text{F} = c/d_\text{o} = 11\,\text{GHz}$. Since the line width of the laser is specified to be better than 150 kHz, the spectra of the Fabry-Pérot interferometer are resolvable for any reasonable finesse. The laser is used at a fixed output power of 3.5 mW for all measurements. Its wavelength is tuned with an analog input to record 0.03-nm-wide spectra. Several of those spectra are measured with different central wavelengths and put together. Since there is some inaccuracy in the absolute position of the central wavelength, this method can lead to some inaccuracy for the position of each part of the spectrum.

Before each measurement, the interferometer has to be aligned carefully. The output coupler (2) is adjusted to form a parallel beam. For this, the beam diameter is determined with a knife-edge method at two positions and the divergence is calculated from these diameters. The diffraction angle of the beam behind the output coupler is smaller than 1 mrad. For the refinement of the alignment of the setup, light from a HeNe-laser at

a wavelength of 633 nm can be coupled into the fiber, and the photodiode (6) can be replaced by a CCD camera. Since the substrate (4) is mounted onto a three-dimensional translation stage, the CCD camera can be used to ensure that the 600-nm-holes ensemble is imaged at the position of the InGaAs-diode. The red laser beam is aligned such that it hits the substrate perpendicularly. Afterwards, the dielectric mirror (2) is mounted. A reflected interference pattern can be seen, arising from reflections by the gold film and the dielectric mirror. This pattern is used to align the two Fabry-Pérot mirrors parallely. Further refinement of the alignment is done with the tunable infrared laser: A transmission resonance is found by tuning the wavelength. Afterwards, the incoming beam and the substrate (4) are moved until the light power measured with diode (6) is maximal. Note that this is not necessarily the position where the surface of the substrate is in the focus of the microscope objective (5). In the following, the parallelism of the two mirrors is successively optimized for a maximal height of the transmission peak.

3.3 Results

An ensemble of ten 600-nm holes is selected for the following measurements. The setup is aligned and optimized as described in the previous section. Then, a spectrum is recorded by tuning the wavelength of the laser light. The spectrum is shown in Fig. 3.5. A sensitivity of $1\,\mathrm{AW}^{-1}$ of the photodiode is used to calculate the light power P_t impinging onto the photodiode from the measured current. However, since only relative intensities are used in our analysis, the sensitivity of the diode does not play any role afterwards. The transmission coefficient of the input mirror is $T_1 = 4\,\%$, and the central wavelength $\lambda_0 = 1550.00\,\mathrm{nm}$. The spectrum shows nine peaks with a spacing of $\lambda_\mathrm{F} = (0.090 \pm 0.008)\,\mathrm{nm}$.

One single peak from the center of the measurement in Fig. 3.5 is shown in Fig. 3.6. The stability of such a peak is investigated by taking many spectra in a row. A drift of the peak position of 0.008 nm is found in 7 min. For comparison, to take a spectrum as in Fig. 3.5 approximately 3 min are needed.

Each spectrum with the dielectric mirror in place is measured three times. The height of the highest peak is taken from each spectrum. The average of the maximal peak heights is used as the value for the maximal transmission, the standard deviation as its error.

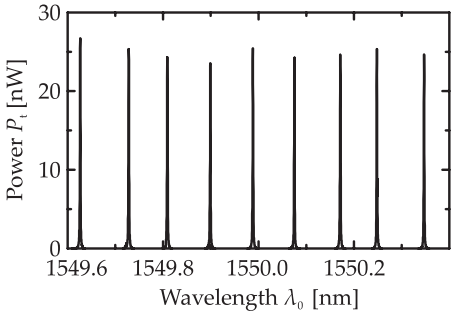

Figure 3.5: Spectrum of light transmitted through ten sub-wavelength holes with a Fabry-Pérot interferometer in the front.

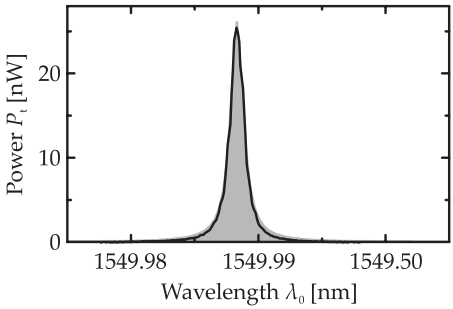

Figure 3.6: Spectrum of a single peak of light transmitted through ten sub-wavelength holes with a Fabry-Pérot interferometer in front. Extract from Fig. 3.5. The gray area illustrates the fit of a Voigt profile.

After removing the dielectric input mirror, spectra at the wavelengths of the previous Fabry-Pérot-transmission peaks are taken. Such a spectrum is shown in Fig. 3.7. This is the spectrum corresponding to the measurement in Fig. 3.5. A small modulation of the transmitted power is found. We take the average transmission of the spectrum as the transmission without mirror. Each spectrum is measured twice. The average is used as a value for the transmission coefficient and its standard deviation as the error.

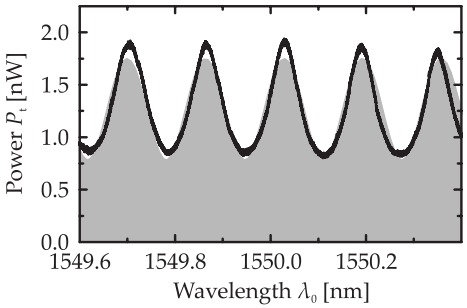

Figure 3.7: Spectrum of light transmitted through ten subwavelength holes without a dielectric input mirror in place. The gray area illustrates the fit of a shifted and scaled cosine curve.

The maximal power with input mirror divided by the average power without the mirror is the enhancement E. The enhancement versus the transmission through the dielectric mirror T_1 is shown in Fig. 3.8. The power transmittance is enhanced by a factor of more than 20 for $T_1 = 7\,\%$. The enhancement is smaller for non-optimal input transmission coefficients T_1.

From each spectrum with input mirror the finesse is determined by dividing the mean distance between two adjacent peaks by the mean full width at half maximum of the peaks. The error is determined from the standard deviation given by the three spectra. Figure 3.9 shows the result. A monotonic decrease is found for the dependence of the finesse F on the transmission coefficients T_1 of the dielectric mirror. The finesse F is bigger than $F = 80$ for very small T_1 and is smaller than $F = 20$ for $T_1 > 40\,\%$.

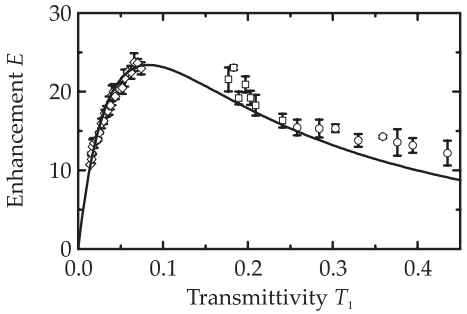

Figure 3.8: Enhancement E versus transmission coefficient of the dielectric mirror T_1, due to the Fabry-Pérot interferometer. The three different symbols (♢,□,○) indicate the three different mirrors used. The solid line is a fit of Eq. (3.6) with $F_1 = 105$.

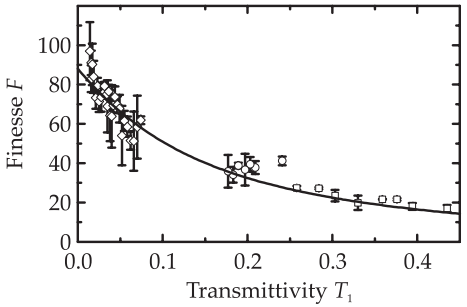

Figure 3.9: Finesse F versus transmittance of the dielectric mirror T_1 of the Fabry-Pérot interferometer. The three different symbols (♢,□,○) indicate the three different mirrors used. The solid line is a calculated curve based on Eq. (3.4) for $F_1 = 105$.

3.4 Discussion

3.4.1 Interpretation of experimental data

Looking at the spectra, we find that the basic assumptions of section 3.1 are fulfilled: The spectrum with input mirror in Fig. 3.5 can be described as a chain of Voigt profiles, as can be seen from the fit in Fig. 3.6. If the mirror is removed, a small modulation remains due to the reflecting surface of the fused silica substrate. This can be seen in Fig. 3.7. The gray area is a fit of $y = P_1(1 + m\cos[P_2(\lambda - \lambda_0)])$ to the experimental data, where P_1 and P_2 are fit parameters. There, $m = 0.38 \pm 0.01$ is found. This is very close to what is expected by the Fresnel formula for an index of refraction of $n = 1.45$: $m = 0.36$.

The irregular distance of the peaks in Fig. 3.5 can be explained by instabilities of the experimental setup. These instabilities are not expected to have any significant influence on the finesse or the enhancement measurements.

By placing a dielectric input mirror in front of a metal film with a subwavelength hole, the transmission can be enhanced by a factor of more than $E = 20$. This is shown by Fig. 3.8. The maximum of the enhancement is found at a transmission coefficient of the input mirror of $T_1 \approx 7\,\%$. A fit of the theoretical curve Eq. (3.6) is shown in the graph. For this curve, the input transmission coefficient T_1 is corrected according to Eq. (3.7). Thus the reflectivity of the glass substrate is taken into account. For the gold film a reflectivity of $R_2 = 0.98$ is assumed, corresponding to the experimental value. The only fit parameter is the limiting finesse F_l. The best fit is found for $F_\mathrm{l} = 105 \pm 5$. A very good agreement between the experimental data and the fit curve can be seen.

The theoretical considerations of the dependence of the finesse on the input transmission coefficient T_1 are tested by comparing the experimental and the calculated finesse. This is shown in Fig. 3.9. The same limiting finesse $F_\mathrm{l} = 105$ as in Fig. 3.8 is used. Again, excellent agreement is found.

The error bars in Fig. 3.8 and Fig. 3.9 are determined from three different measurements and their standard deviation. Comparing the error bars and the deviation of data points from the fit curve, the error estimation seems reasonable. However, for large input transmission coefficients the enhancement tends to be bigger than the theoretical predictions.

3.4.2 Substantiating the theoretical considerations

For the calculations the input transmission coefficient T_1 is corrected by Eq. (3.7). Thus the reflectivity of the system is increased to account for the surface of the glass substrate. The transmission coefficient decreases, and the theoretical curves in Fig. 3.8 and Fig. 3.9 are stretched in the T_1-axis by 30–40 %. To test this assumption, we numerically evaluate the transmission and the finesse of two coupled Fabry-Pérot interferometers. The first interferometer is formed by the input mirror and the glass surface, and the second interferometer is formed by the glass substrate and the gold film. The whole transmission curve is convolved with a Gauss curve to simulate the effect of a real interferometer. It is found that Eq. (3.7) is a good approximation for calculating the enhancement, but the correction factor Eq. (3.4) seems to slightly overestimate the effect on the finesse.

The influence of surface imperfections, misalignment and other error sources is simulated by convolving the amplitude transmission function with a Gauss curve leading to a chain of Voigt profiles for the transmission. However, the source and the form of the remaining errors are not known and might deviate form a Gauss curve. So some uncertainty remains for substantiating the theoretical curves. But still, the theoretical considerations describe the experimental finesse F and the enhancement E very well.

3.4.3 Further improvements

The theoretical analysis seems to be founded well enough to analyze the potential for further improvements: If, by further optimization, the limiting finesse can be increased, the resulting maximal enhancement is determined just by the absorption in the gold film, which is experimentally found to be about 2 % for an optically thick film. Using this value we find that the enhancement would reach values of $E = 50$ at $T_1 = 2\,\%$ and an effective finesse of $F_e = 155$. An absorption of 2 % is, what is expected from the Fresnel formula [12] and from literature values of the complex index of refraction for gold at $\lambda_0 = 1550\,\text{nm}$ [42]. Literature values for silver [42] lead to an absorption coefficient below 1 %, though much more care in preparing and handling the sample would be needed to prevent degradation of the surface [43]. For $R_2 = 0.99$ the enhancement could reach values of $E = 100$ at $T_1 = 1\,\%$ and $F_e = 313$.

The Fabry-Pérot enhanced transmission through sub-wavelength holes

can be applied to other wavelengths. E.g., literature values predict reflection coefficients for silver above $R_2 = 0.98$ at a wavelength of $\lambda_0 = 500\,\text{nm}$. Therefore, an enhancement of $E = 50$ should be reachable at wavelengths in the visible part of the optical spectrum. Reflection coefficients above $R_2 = 0.99$ are achievable at Terahertz wavelengths [44]. However, fabrication of a high-quality input mirror is a challenging task [45]. Thus, an enhancement comparable to the value for infrared or optical wavelengths might be expected.

The method described in this chapter can be used to enhance the transmission through other sub-wavelength structures and can be combined with other methods to enhance the transmission through such nano-apertures. As already mentioned in the introduction, the transmission through sub-wavelength holes can be enhanced by a factor of 10 by appropriate structuring [9]. Combining this with the Fabry-Pérot enhanced transmission technique, three orders of magnitude of transmitted power can be gained. The Fabry-Pérot enhanced transmission should be applicable to optical wavelengths using silver instead of gold films. Furthermore, it can be applied in more complicated situations, e.g., using a spherical dielectric mirror instead of a plane-parallel mirror. Therewith, the wave, which is going to be transmitted through the hole, could simultaneously be focused onto the hole.

3.5 Summary

We conclude that using a dielectric mirror in front of a metal surface with a sub-wavelength hole in it, the power being transmitted through the hole is enhanced by a factor of more than 20. Theoretically, a factor of 100 is reachable by further optimization. The technique described herein is very simple and flexible and thus may become a useful tool to reach the efficiencies needed for many real-life applications of sub-wavelength structures in optics.

Chapter 4

Holographic phase conjugation through sub-wavelength holes

In the previous chapter 3 a method to enhance the transmission through sub-wavelength holes is introduced: Increasing the intensity before the hole with a Fabry-Pérot interferometer augments the transmission. Another possibility to obtain a better efficiency for transmitting light through sub-wavelength structures is efficient addressing. The simplest method to do so is focusing with a lens or a microscope objective. However, these conventional focusing devices either have a small numerical aperture or a small field of view. For a good combination of these values considerable efforts have to be made to compensate for imaging errors. Thus, in this chapter we investigate a holographic lens as an alternative method to focus light.

Holographic lenses are already tested for some applications, see, e.g., [46]. There, a hologram is recorded with a signal wave, which is coming from a lens, and a plane reference wave. Read out is done by illumination with the plane reference beam. The light wave of the original lens is then reconstructed. Usually, the numerical aperture in these systems is not very high.

Holography is not only able to reconstruct a recorded wavefront, but also the back-propagating wave can be generated by phase-conjugated read-out. In this case, the hologram is recorded by a plane reference wave R and a more complicated signal wave S. For read-out, the phase-conjugated reference beam is used, i.e., a plane wave R^* counter-propagating to the original reference beam R. This leads to reconstruction of the phase-conjugated signal beam S^*. Phase conjugation has already been used, e.g.,

for advanced holographic data storage [47], for image correlation [48], and imaging through scattering media [49].

It is straightforward to combine phase conjugation with holography of focused waves in order to get holographic focusing. There is already solid knowledge available from literature about holographic recording with focused waves. E.g., a method to multiplex many holograms in a photosensitive medium, which uses spherical reference beams, is the so-called shift multiplexing [50]: The interference pattern of a spherical reference beam coming from a high-numerical-aperture microscope objective and a plane signal wave is recorded. The signal wave is reconstructed by readout with the spherical reference beam. The efficiency of reconstruction depends strongly on the position of the microscope objective. Thus, by shifting the objective or the recording medium, many holograms can be multiplexed conveniently.

Another example, which is the closest to the present study, are experiments with a scanning near field optical microscope (SNOM) [51]. There, the interference pattern resulting from the light coming from a subwavelength tip of a SNOM and a plane reference wave, is holographically recorded. The focus of these SNOM experiments is on phase-conjugating the evanescent waves being emitted from a sub-wavelength tip. In contrast, we use the propagating waves being emitted from a sub-wavelength source to create a focusing apparatus as close as possible to the diffraction limit.

In the microwave-regime phase-conjugation has been shown to be able to reconstruct features on the sub-wavelength scale [52]. In this experiment, random scatterers were placed in proximity to the microwave source. Evanescent waves being emitted from the source are scattered into propagating waves. The combined field is then phase-conjugated. The reconstructed beams are scattered into evanescent waves which are now detected by an antenna. By this method, sub-wavelength focusing has been shown. However, this method is somehow analogous to a SNOM, i.e., by placing a probe close to an object, sub-wavelength information can be extracted.

In this chapter, we study holographic recording of light in the visible range through tiny holes drilled into a metal film, which is situated on top of a photosensitive material. Phase-conjugated read out is supposed to focus the light back on the holes. Open questions are, how well this method works and what the limitations are.

Figure 4.1 shows how a high-numerical-aperture holographic lens func-

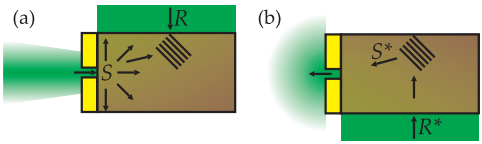

Figure 4.1: Scheme of holographic focusing of light: (a) A hologram is written with a plane reference wave R and a signal wave S coming from a sub-wavelength hole acting as a point source. The lines indicate one of many index-of-refraction gratings present in the crystal after recording. (b) The hologram is read-out with the phase-conjugated signal wave R^*. The phase-conjugated signal wave S^* is reconstructed.

tions: Light passing through a sub-wavelength hole in an optically thick, i.e., intransparent, metal film acts as a signal wave S and interferes with a plane reference beam R. In a photosensitive material this interference pattern is recorded as a modulation of the index of refraction. When the material is illuminated with the phase-conjugated reference beam R^*, the phase-conjugated signal beam S^* is reconstructed. Since the signal wave S is strongly diffracted into the crystal, S^* now propagates towards the sub-wavelength hole. In principle, waves from all directions in the half sphere behind the hole can contribute to the focus. Thus, a numerical aperture very close to the index-of-refraction of the material can result.

4.1 Background

A hologram is an absorption or an index-of-refraction pattern, which stores the interference of a signal wave S and a reference wave R. The well-known photorefractive effect in iron-doped lithium niobate crystals can be used to record the interference pattern [53]. These crystals are chosen, because they are commercially available at good optical quality and offer a strong photorefractive effect. Furthermore, material parameters and the photorefractive process of lithium niobate crystals are well understood.

However, for holography through sub-wavelength holes certain peculiarities arise: The signal wave is a wave being transmitted through a sub-wavelength hole, and hence, due to diffraction, the intensity, the propagation direction and the polarization are inhomogeneous in the crystal

volume. As consequences, the interference pattern exhibits several different grating vector directions, unusual elements of the material tensors become relevant and the geometry of the diffraction problem differs from the transmission and reflection geometry which are considered by Kogelnik [54].

In this section a general, tensorial treatment of the photorefractive effect is provided. Literature values for the material tensors are used to estimate the strength of diffraction at different positions in the crystal. Furthermore, diffraction from these gratings is discussed.

4.1.1 Photorefractive effect in iron-doped lithium niobate crystals

The photorefractive effect changes the refractive index according to an inhomogeneous light distribution. At continuous-wave intensities photorefraction in iron-doped lithium niobate crystals is described by the one-center model [55]: Iron atoms act as charge centers in lithium niobate crystals, where they exist in two valence states: Fe^{2+} and Fe^{3+} [56]. Incoming photons, which are absorbed, excite electrons from the Fe^{2+} states into the conduction band. There, they are redistributed due to three major current sources: The bulk photovoltaic current $\boldsymbol{j_{\mathbf{phv}}}$, the drift current $\boldsymbol{j_{\mathbf{drift}}}$, and the diffusion current $\boldsymbol{j_{\mathbf{diff}}}$. Thus the total current density in the crystal is:

$$\boldsymbol{j} = \boldsymbol{j_{\mathbf{phv}}} + \boldsymbol{j_{\mathbf{drift}}} + \boldsymbol{j_{\mathbf{diff}}}. \tag{4.1}$$

The redistributed electrons are trapped by Fe^{3+} states. An electrical space-charge field E_{SC} builds up due to the charge redistribution, and the refractive index is changed according to the linear electro-optic effect.

Excitation and recombination of electrons to and from the conduction band are described by rate equations [57]. For continuous wave laser light an adiabatic approximation is made [53]. Additionally, it can be assumed that the density of sources and traps is sufficiently high so that no space-charge limiting effects arise. Then, the density of electrons in the conduction band is proportional to the light intensity I and the absorption α in the crystal. The absorption can show a small dependence on the polarization of the crystal. If $\boldsymbol{A}$ is an electric field vector of the impinging light wave, normalized to the intensity I such that $|\boldsymbol{A}|^2 = I$, the number of electrons in the conduction band is [58]:

$$N_{\mathrm{e}} = \gamma_{lm} A_l A_m. \tag{4.2}$$

Here and in the following the sum convention is used for repeating indices. The tensor γ_{lm} depends on the wavelength of the impinging light and the doping and oxidization state of the crystal.

Electrons excited to the conduction band increase the conductivity of the material by several orders of magnitude. By applying an electric field $\boldsymbol{E}$ an Ohmic drift current $\boldsymbol{j_{\text{drift}}}$ results. The direction of this current depends on the mobility tensor μ_{lm} and might differ from the direction of the electric field. Thus the drift current is [53]:

$$j_{\text{drift},l} = q_e N_e \mu_{lm} E_m = q_e \gamma_{op} A_o A_p \mu_{lm} E_m = \sigma_{lm} I E_m. \tag{4.3}$$

Here $\sigma_{lm} = q_e \gamma_{op} A_o A_p \mu_{lm} / I$ is the tensor of the specific photoconductivity and depends on the polarization and wavelength of the incoming light wave and on crystal parameters. The anisotropy of σ_{lm} is known in $BaTiO_3$ and in $KNbO_3$ [59]. Unfortunately, the anisotropy is unknown in lithium niobate. Thus, usually an isotropic specific photoconductivity with σ_{33} is assumed.

For an inhomogeneous illumination a diffusion current $\boldsymbol{j_{\text{diff}}}$ due to the gradient of mobile charge carriers in the conduction band arises:

$$j_{\text{diff},l} = k_B T \mu_{lm} \partial_m N_e = \frac{k_B T}{q_e} \partial_m \left(\sigma_{ml} I\right) \tag{4.4}$$

The bulk photovoltaic current relies on the lack of the inversion symmetry in lithium niobate crystals: Electrons excited to the conduction band show a net redistribution approximately along the c-axis of the crystal [60]. This effect depends on the intensity and polarization of the incoming light wave and can be described by a third rank tensor β_{lmo} [61]. Then the components of the bulk photovoltaic current density $\boldsymbol{j_{\text{phv}}}$ are:

$$j_{\text{phv},l} = \beta_{lmo} A_m A_o^*, \quad \beta_{lmo} = \beta_{lom}^*, \tag{4.5}$$

where * denotes complex conjugation. The bulk photovoltaic tensor β_{lom} depends on the doping and oxidization state of the crystal. Though it has complex entries, the current $\boldsymbol{j_{\text{phv}}}$ is always real as $\beta_{lmo} = \beta_{lom}^*$. However, the complex phase of the entries becomes relevant for a periodic light pattern, where the phase of the current pattern can be shifted with respect to the interference pattern. Non-zero entries of β_{lmo} for $m \neq o$ are $\beta_{112} = \beta_{121}$ and $\beta_{123} = \beta_{132}^* = \beta_{113} = \beta_{131}^*$. These off-diagonal entries make anisotropic recording of holograms possible: Two perpendicularly polarized

waves can write a hologram by their polarization grating though no intensity pattern occurs [62].

If the light wave imping onto the crystal is known, the resulting space-charge distribution ρ can be calculated using the continuity equation

$$\partial_l j_l = -\partial_t \rho, \tag{4.6}$$

where ρ is the charge density and t is the time since beginning of the recording. Furthermore, Gauss' law relates the electric displacement field $\boldsymbol{D}$ and the charge density ρ:

$$\partial_l D_l = \rho. \tag{4.7}$$

The displacement field $\boldsymbol{D}$ and the corresponding electric field $\boldsymbol{E}$ are related in a non-trivial way as the electric field distorts the crystal structure, which changes the effective dielectric tensor $\epsilon_{\text{eff},lm}$ [63].

In the general case, these equations have to be solved numerically. An analytical solutions exists for a grating recorded by two plane waves: a plane reference wave described by $\boldsymbol{A_R} \exp(ik_{\text{R},m} r_m)$ and a plane signal wave described by $\boldsymbol{A_S} \exp(ik_{\text{S},m} r_m)$. In this case the interference pattern is sinusoidal and the problem can be reduced to one dimension, where the space-charge field $\boldsymbol{E_{SC}}$, the charge density ρ, and the current $\boldsymbol{j}$ vary periodically along the grating vector $\boldsymbol{K_g} = \boldsymbol{k_S} - \boldsymbol{k_R}$. The space charge field can be described by a scalar E_{SC}. For a small degree of modulation $m_g = 2\left(I_S I_R\right)^{0.5}\left(I_S + I_R\right)^{-1}$, with $I_S = |A_S|^2$, $I_R = |A_R|^2$, the Fourier expansion of E_{SC} and ρ can be truncated after the first Fourier order and an analytical solution is found [57].

Assuming a plane-wave grating is not as limiting as it might seem at first sight: For many applications, the reference and the signal wave vary their amplitude and wave vector on scales which are much larger than a wavelength. In this case a plane-wave grating is a local approximation of the resulting pattern.

For a plane-wave grating the relation between the displacement field $\boldsymbol{D}$ and the electric field $\boldsymbol{E}$ simplifies [64]. Then, the space-charge field E_{SC} is parallel to the grating vector $\boldsymbol{K_g}$. We split the intensity $I = I^{(0)} + I^{(1)}$ into a constant part $I^{(0)}$ and a modulated part $I^{(1)}$. Accordingly, we proceed for E_{SC} and ρ. Then the amplitude of the periodic space-charge distribution $\Delta\rho$ is related to the amplitude of the space-charge field ΔE_{SC} by

$$\Delta\rho = i|\boldsymbol{K_g}|\epsilon_0 \epsilon_{\text{eff}}^{\text{static}} \Delta E_{\text{SC}}. \tag{4.8}$$

Here ϵ_0 is the electric vacuum permittivity and the effective dielectric constant is $\epsilon_{\text{eff}}^{\text{static}} = \epsilon_{\text{S},lm}^{\text{static}} \hat{K}_l \hat{K}_m + B_o A_{op}^{-1} B_p / \epsilon_0$ with $A_{lm} = C_{lqmp}^{\text{E}} \hat{K}_q \hat{K}_p$ and $B_l =$

$e_{mlo}\hat{K}_m\hat{K}_o$. There, $\epsilon^{\text{static}}_{\text{S},lm}$ is the clamped dielectric tensor, $\hat{K}_l = K_{\text{g},l}/|\boldsymbol{K}_\mathbf{g}|$ is the normalized grating vector, C^{E}_{lmop} is the tensor of the elastic constants at constant electric field, and e_{lmo} is the piezoelectric stress tensor.

Furthermore, we assume that the electric field is short cut and thus $E^{(0)} = 0$. Now, solving the system of equations (4.1), (4.6), and (4.8), we get up to the first Fourier order of the resulting electric field grating E [57]:

$$E^{(1)}(\boldsymbol{r}, t) = \frac{1}{2}\left(\Delta E_{\text{SC}} \mathrm{e}^{iK_{\text{g},m}r_m} + \text{c.c.}\right)\left(1 - \mathrm{e}^{-t/\tau}\right), \tag{4.9}$$

with

$$\Delta E = m_\text{g} \frac{K_{\text{g},l}\beta_{lop}\hat{A}_{R,o}\hat{A}^*_{S,p} + i(k_\text{B}T/q_\text{e})K_{\text{g},l}K_{\text{g},m}\sigma_{lm}\hat{A}_{R,o}\hat{A}^*_{S,o}}{K_{\text{g},l}K_{\text{g},m}\sigma_{lm}/K_\text{g}}, \tag{4.10}$$

and

$$\tau = \frac{\sigma_{lm}K_{\text{g},l}K_{\text{g},m}I^{(0)}}{K^2_\text{g}\epsilon_0\epsilon^{\text{static}}_{\text{eff}}}. \tag{4.11}$$

Here, $\hat{A}_{R,p} = A_{R,p}/|\boldsymbol{A}_\mathbf{R}|$ and $\hat{A}_{S,p} = A_{S,p}/|\boldsymbol{A}_\mathbf{p}|$. According to Eq. (4.9–4.11), the electric field builds up exponentially and saturates at a sinusoidal field which, due to its complex phase, may be phase-shifted with respect to the interference pattern.

The most prominent situation in holography is a plane-wave grating with a grating vector $\boldsymbol{K}_\mathbf{g}$ parallel to the z-axis of the crystal, and a beam linearly polarized along the x-axis. In this case the formula simplify to:

$$E^{(1)}(\boldsymbol{r}) = \left[m_\text{g}\frac{\beta_{311}}{\sigma_{33}}\cos\left(K_{\text{g},m}r_m\right) + m_\text{g}(k_\text{B}T/q_\text{e})|\boldsymbol{K}_\mathbf{g}|\sin\left(K_{\text{g},m}r_m\right)\right]\left[1 - \mathrm{e}^{-t/\tau}\right], \tag{4.12}$$

with

$$\tau = \frac{\sigma_{33}I^{(0)}}{\epsilon_0\epsilon^{\text{static}}_{\text{eff}}}. \tag{4.13}$$

The first term in Eq. (4.12) describes a grating recorded due to the bulk photovoltaic effect, whereas the second term is recorded by diffusion and is phase-shifted by $\pi/2$ with respect to the interference pattern. The diffusion grating can be neglected in most practical applications due to the strong photovoltaic effect in lithium niobate crystals.

The modulation of the electric space-charge field ΔE_{SC} increases with the degree of modulation of the interference pattern m_g. Thus, in reality one often tries to record holograms near $m_\text{g} = 1$, to increase the hologram

strength. But for high modulations the resulting electric field pattern is no longer sinusoidal and higher harmonics begin to play a role. Numerical simulations indicate that the first harmonic of the electric field pattern is approximately twice as high for $m_g = 1$ compared with the linear theory [65]. The difference quickly drops for smaller m_g. Additionally, the recording time τ is supposed to slightly increase with m_g [66]. In practice a degree of modulation larger than $m_g = 0.8$ is unreachable because of some background illumination so that the linear approximation probably is a quite good one.

4.1.2 Change of the dielectric constant

Due to the modulated electric field which builds up because of the photorefractive effect, the dielectric tensor ϵ_{kl} changes according to [63]:

$$\Delta\epsilon^{-1}_{\mathrm{eff},lm} = r_{\mathrm{eff},lm}\Delta E_{\mathrm{SC}}. \tag{4.14}$$

From this, we can calculate [67]:

$$\Delta\epsilon_{\mathrm{eff},lm} = \epsilon_{lo}\left(r_{\mathrm{eff},op}\Delta E_{\mathrm{SC}}\right)\epsilon_{pm}. \tag{4.15}$$

In the above equations the following identity is used:

$$r_{\mathrm{eff},lm} = r_{\mathrm{S},lmo}\hat{K}_o + p_{\mathrm{E},lmop}\hat{K}_p A^{-1}_{o,q} B_q. \tag{4.16}$$

The tensors are: p_{E}, the elasto-optic Pockels tensor and r_{S}, the electro-optic Pockels tensor.

The effective opto-electric tensor $r_{\mathrm{eff},lm}$ incorporates crystal deformations due to the electric fields. The difference is small for gratings parallel to the c-axis but becomes more pronounced for other directions.

4.1.3 Diffraction from volume holograms

The previous sections describe how periodic space-charge fields are recorded locally due to the photorefractive effect leading to a periodic modulation of the dielectric tensor. That way, the index of refraction of the iron-doped lithium niobate crystal is modulated according to the interference pattern of the signal and the reference wave. When the index-of-refraction pattern is illuminated with the reference wave, the signal wave is reconstructed, due to the holographic principle [68].

Gratings recorded by two plane waves can be classified according to their geometry. Three types are usually discussed: First, the transmission geometry, where both, the reference and the signal wave, enter the crystal from the same surface. Second, the reflection geometry, where R and S enter from opposite surfaces. And third, the 90°-geometry, where two beams enter perpendicularly from different surfaces. The three geometries are explained in Fig. 4.2.

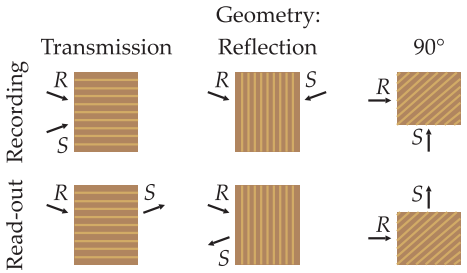

Figure 4.2: Holography in transmission, reflection, and 90°-geometry.

The holographic principle does not only apply to the case where the hologram is read-out by the reference beam R, but also to phase-conjugated read-out. If the hologram is illuminated with the phase-conjugated reference beam R^*, instead, the phase-conjugated signal wave is reconstructed. For a plane wave, the phase-conjugated wave is simply the counter-propagating plane wave. More generally, phase conjugation reconstructs a back-propagating wave. Fig. 4.3 compares direct and phase-conjugated read-out of a hologram.

For efficient diffraction the Bragg-condition for the read-out wave vector $\boldsymbol{k_p}$ and the diffracted wave $\boldsymbol{k_d}$ has to be fulfilled:

$$\Delta \boldsymbol{k} = \boldsymbol{K_g} + \boldsymbol{k_p} - \boldsymbol{k_d} = 0. \tag{4.17}$$

Or for phase-conjugated read-out:

$$\Delta \boldsymbol{k} = -\boldsymbol{K_g} + \boldsymbol{k_p} - \boldsymbol{k_d} = 0. \tag{4.18}$$

The maximal diffraction efficiency is determined by the coupling constant κ

$$\kappa = \frac{1}{4}\frac{2\pi}{\lambda}\frac{\Delta\epsilon}{\epsilon}, \tag{4.19}$$

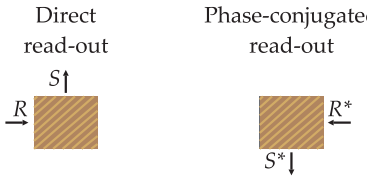

Figure 4.3: Direct and phase-conjugated read-out.

where λ is the wavelength in the crystal. It is assumed that no absorption occurs. When the Bragg condition is fulfilled, the theoretical diffraction efficiency for transmission, reflection [54], and 90°-geometries [69], are:

$$\begin{aligned} \eta &= \sin^2\left(\kappa d / cos(\nu)\right), \\ \eta &= \tanh^2\left(\kappa d / cos(\nu)\right), \quad \text{and} \\ \eta &= 1 - J_0^2\left(2\kappa d\right) - J_1^2\left(2\kappa d\right), \end{aligned} \tag{4.20}$$

respectively. In the 90°-geometry with a width of the reference beam W_R and of the signal beam W_S it is $d = (W_R W_S)^{0.5}$. For the transmission and the reflection geometry d is the thickness of the material. In the crystal, ν is half the angle between the propagation direction of the signal and the reference wave. The different curves for Eq. (4.20) are plotted in Fig. 4.4. There $\nu = 0$ is set for the 90° geometry. As can be seen, the diffraction efficiency is very well described by a quadratic increase for diffraction efficiencies below 20 %. For larger normalized lengths $\kappa d / \cos(\nu)$ the diffraction efficiency becomes sub-quadratic as the read-out wave is depleted. For the transmission geometry the light power periodically oscillates between the signal and the reference wave, leading to a $\sin^2$ behavior. This cannot happen in the reflection geometry. The 90°-geometry shows an intermediate behavior, which, like the reflection geometry, is monotonically increasing.

The quadratic approximation is applicable when pump depletion can be neglected. In this case, the amount of light diffracted from each part of the crystal is constant, and interferes constructively at the exit face of the crystal. Thus, the electric field of the diffracted light depends linearly on the crystal thickness. And the diffracted light intensity depends quadratically on the thickness.

When the Bragg-condition is slightly violated, for example because of an angular detuning $\Delta\nu$ of the read-out wave, the diffraction efficiency

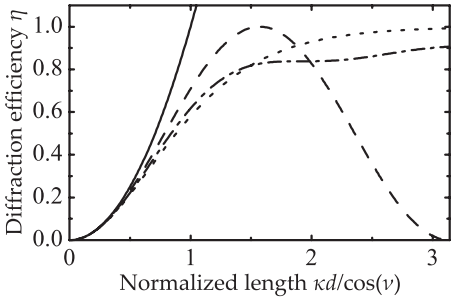

Figure 4.4: The diffraction efficiency η for the first-order approximation (solid line), transmission (dashed line), reflection (dots) and 90°-geometry (dot-dashed line) versus the normalized length $\kappa d/\cos(\nu)$.

drops. In the limit of small diffraction efficiencies, where pump depletion can be neglected, the angular selectivity shows a $\mathrm{sinc}^2(\text{const.}\,\Delta\nu)$ behavior, with the first zero at [54]

$$\Delta\nu = \frac{\lambda}{d} \tag{4.21}$$

for transmission geometry. For the 90°-geometry the first zero is found at [69]:

$$\Delta\nu = \frac{\lambda}{W_\mathrm{R}}. \tag{4.22}$$

First-order approximation

The coupled wave equations can be solved analytically for gratings written by two plane waves. For more sophisticated holograms, where the diffraction efficiency fulfills $\eta \ll 1$, the first-order Born approximation, a linear approximation, can be used: The inhomogeneities of the dielectric constant act as point sources for the scattered wave. The superposition of all spherical waves emitted from the point sources is the scattered wave [12]:

$$A_\mathrm{d}(\boldsymbol{r}) = \left(\frac{2\pi}{\lambda_0}\right)^2 \int \mathrm{d}^3\boldsymbol{r}' \frac{\mathrm{e}^{ik|\boldsymbol{r}-\boldsymbol{r}'|}\mathrm{e}^{-(\alpha/2)|\boldsymbol{r}-\boldsymbol{r}'|}}{4\pi|\boldsymbol{r}-\boldsymbol{r}'|} \epsilon^{(1)}(\boldsymbol{r}') A_\mathrm{p}(\boldsymbol{r}'). \tag{4.23}$$

Here, $A_d(\boldsymbol{r})$ is the diffracted wave, $A_p(\boldsymbol{r'})$ the read-out wave, λ_0 is the vacuum wavelength, and $k = 2\pi(\epsilon^{(0)})^{0.5}/\lambda_0$. Several approximations have to be made for the above formula to be valid: First an isotropic material is assumed and vectorial effects are neglected. Vectorial and anisotropic versions of the Born approximation exist [70], and these effects are discussed in the next section. The second assumption is that the amount of diffracted light is so small that diffraction of the diffracted light can be neglected. This is the same assumption as for the quadratic increase of the diffraction efficiency in Fig. 4.4. Within this approximation Eq. (4.23) allows the calculation for more complicated holograms.

Direct integration of Eq. (4.23) demands high amounts of calculation time and memory capacity, as, generally, a grid spacing smaller than the wavelength of the light has to be chosen. Equation (4.23) can be interpreted as the convolution of the Green's function and the product of the incoming field and the modulation of the dielectric constant. A convolution can be efficiently evaluated using the Fast Fourier Transformation (FFT) [71]. Using the peculiarities of volume holograms the calculation speed can be further drastically enhanced [72]. For plane-wave gratings the integral can be evaluated analytically [73]. And with further assumptions the integral can be analytically evaluated in many more cases. As we see in a later section, an analytical evaluation is also possible for holographic phase-conjugation of a point source.

Vectorial effects

Diffraction from a volume grating becomes a complicated problem for the general anisotropic, vectorial case. Different polarization states may couple and the coupled wave equations become a system of four or more equations [74]. The polarization of the diffracted wave may be completely different from that of the original signal wave. Additionally, the polarization of waves may change as they propagate because of the birefringence of the medium. Although theories exist for those cases, they are complicated and elaborate. The same is true for anisotropic, vectorial versions of the first-order Born approximation [70].

However, in the case of a volume hologram the situation simplifies due to the phase-matching condition Eq. (4.17,4.18). The propagation vectors of the read-out wave $\boldsymbol{k_p}$, the diffracted wave $\boldsymbol{k_d}$, and the grating vector $\boldsymbol{K_g}$ have to fulfill the Bragg condition $\Delta\boldsymbol{k} = 0$, for efficient diffraction. This phase-matching condition imposes restrictions on the polarization state of

the diffracted wave. For the case of a hologram, the condition is always fulfilled, if the read-out wave is close to the phase-conjugated reference wave: $\boldsymbol{k_P} = -\boldsymbol{k_R}$ and the polarization of the diffracted wave is the same as the one of the phase-conjugated signal wave. The diffracted wave might change the polarization as it propagates through the crystal. However, since S^* is exactly the back-propagating signal wave, the phase-conjugated signal wave is reconstructed at the hole.

Thus, when calculating the diffracted wave, we assume that at each point the polarization state of the diffracted wave is the phase-conjugated one of the signal wave, also at the exit surface of the crystal. The coupling constant for known polarization states can be found in the literature [58]. There it is derived for the coupled wave equations. But, as we have seen before, by analogy the coupling constant can be applied to the Born approximation as well:

$$\Delta\epsilon_{\text{eff}} = -\hat{A}_{S,l}\Delta\epsilon_{\text{eff},lm}\hat{A}_{R,m} \tag{4.24}$$

with $\Delta\epsilon_{\text{eff},lm}$ from Eq. (4.15). Thus, if vectorial effects at the reconstruction site are neglected, Eq. (4.23) can be applied directly. We call this the pseudo-vectorial calculation. Alternatively a vector valued $\Delta\boldsymbol{\epsilon_{\text{eff}}}$ can be assumed where the direction of polarization depends on the polarization of the emitted signal wave S.

The approximation made herein assumes that the crystal and the birefringence are large enough so that the Bragg-condition has to be strictly fulfilled. If a wave is propagating along the c-axis, the index of refraction for both polarization directions is the same, and phase-matching is automatically fulfilled. If the coefficients of the dielectric tensor allow coupling of the two polarization states, the original polarization might not be maintained. However, in the geometry we choose we do not expect this effect to be relevant.

4.1.4 Holographic scattering

Holographic scattering describes the photorefractive amplification of light being scattered by surface defects or defects in the bulk of the crystal [75]. In a photorefractive crystal a pump wave and scattered light can interfere and record gratings which are shifted with respect to the interference pattern and which are self-amplified and diffract more and more of the pump light into scattered waves [76]. In our experimental configuration, where

the crystal is illuminated with ordinarily polarized light, anisotropic scattering is dominating [77]. This means that the scattered light is extraordinarily polarized. In lithium niobate the β_{132} and β_{123} elements of the bulk photovoltaic tensor are responsible for anisotropic scattering due to their large imaginary values [78]. The imaginary value leads to a grating shifted by $\pi/2$ with respect to the interference pattern ensuring efficient coupling of the pump wave and the scattered wave.

4.2 Methods

In this section we discuss the iron-doped lithium niobate samples, the optical setup, and the measurement procedure for holographic phase-conjugation through a sub-wavelength hole.

4.2.1 Sample crystal

Iron-doped lithium niobate crystals are used as the photosensitive material. The doping level is 0.05 weight % Fe_2O_3 in the melt. The crystals are cut into $W_x \times W_y \times W_z = 1 \times 8 \times 4\,\mathrm{mm}^3$ sized pieces, and the surfaces are polished. To check the quality of the surface polishing, the topography of the x-surface of one crystal is measured with an interferometer. Figure 4.5 shows the results: The surfaces have a planarity of about 3λ. There might be a small wedge angle between the two surfaces, which is not seen by the interferometer. Absorption measurements with a Varian Cary 500 spectrometer reveal absorption coefficients for ordinarily polarized light of $\alpha = (560 \pm 10)\,\mathrm{m}^{-1}$ at a vacuum wavelength $\lambda_0 = 532\,\mathrm{nm}$ and $\alpha = (625 \pm 10)\,\mathrm{m}^{-1}$ at $\lambda_0 = 514\,\mathrm{nm}$. Using the absorption coefficient at $\lambda_0 = 477\,\mathrm{nm}$ the oxidization state is found to be: $c_{\mathrm{Fe}^{2+}}/c_{\mathrm{Fe}^{3+}} = 0.09$ [56].

A $(280 \pm 30)\,\mathrm{nm}$ thick gold film is evaporated onto the z-face of the crystal. Gold is used because it has a reasonable optical thickness at 532 nm and is not as sensitive to degradation as silver [43]. A cross section as seen with a scanning electron microscope of a gold film on lithium niobate is shown in Fig. 4.6. The cross-section is made with a focused ion beam.

A focused-ion beam is also used to fabricate holes with diameters of 50 –1000 nm into the gold film. See Fig. 4.7 for the positions of the different holes on the crystal surface. Figure 4.8 shows a top view of a hole and Fig. 4.9 a cross section. The holes have a circular shape and are slightly conic over the depth of the gold film due to the fabrication.

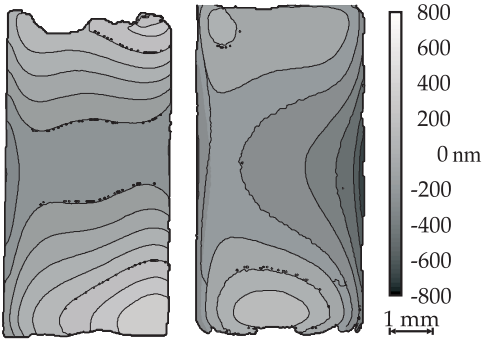

Figure 4.5: Topography of the $+x$ and $-x$-surface of the crystal.

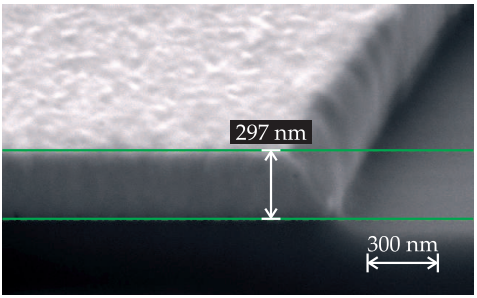

Figure 4.6: Cross section through a 297-nm-thick gold film on a lithium niobate crystal. (Photo: A. Sehrbrock, Forschungszentrum caesar)

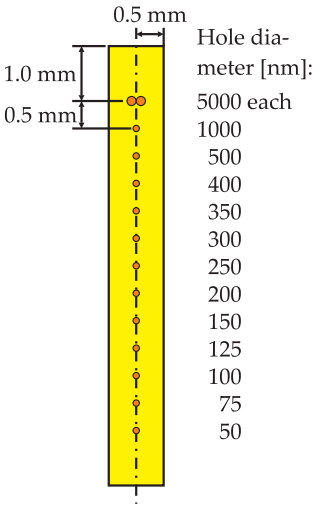

Figure 4.7: Layout of the sub-wavelength holes on the z-surface of the lithium niobate crystal.

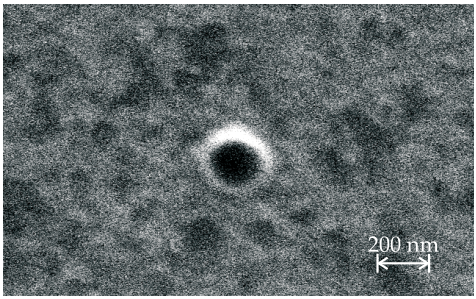

Figure 4.8: Top view of a 200-nm hole in a gold film on top of a lithium niobate crystal. The picture is made with a focused ion beam. (Photo: A. Sehrbrock, Forschungszentrum caesar)

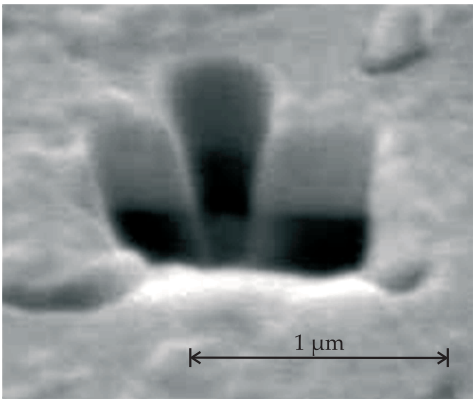

Figure 4.9: Electron microscopy picture of the metal surface with a hole in it. With a focused ion beam, a cross section is made to study the shape of the hole. (Photo: A. Sehrbrock, Forschungszentrum caesar)

4.2.2 Optical setup

The 90°-geometry is used to record the holograms. Figure 4.10 shows the orientation of the crystal and the involved light beams. The *c*-axis (*z*-direction) of the lithium niobate crystal is oriented parallel to the incoming signal beam S. The reference beam R and the phase-conjugated reference beam R^* are oriented anti-parallel and parallel to the *x*-axis. The electric field vector of the incoming light is aligned along the *y*-axis. The surfaces which are not exposed to light are covered with silver to short-circuit the *z*-surfaces and *y*-surfaces of the crystal.

Figure 4.11 shows the experimental setup. Light from a frequency-doubled Nd:YAG laser with a wavelength of 532 nm is split into three beams: The signal beam S, the plane-wave reference beam R and the phase-conjugated reference beam R^*. Using a $\lambda/2$-wave plate (1) the electric field vector is polarized perpendicularly to the optical table. Beam blockers (2) are used to switch between recording and read-out mode. During recording, the signal beam passes through a spatial frequency filter (3) to obtain a beam diameter adapted to the microscope objective (4). This objective focuses the light onto the sub-wavelength hole in the metal

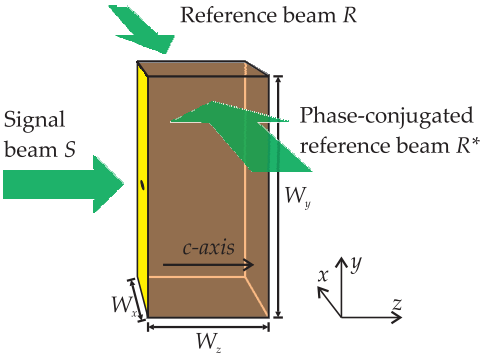

Figure 4.10: Crystal orientation. The light is polarized parallel to the y-axis.

film on the lithium niobate crystal (5). The back-reflections of the reference and signal beams interfere at the photodiode (6). This signal is used to stabilize the relative phase between the two beams via a mirror (7) mounted on a piezo-mechanical translator. During read-out, the phase-conjugated light is periodically modulated with a mechanical chopper (8). The phase-conjugated signal beam is detected with a photodiode (9), and a lock-in technique is employed to increase the sensitivity. Furthermore, two computer-controlled motors are used to rotate the read-out beam in the plane of the table (10) and perpendicularly to it (11) to check the angular selectivity of the holograms.

A special mount is designed to fix the crystal. Fig. 4.12 shows a picture of the device. The crystal holder is placed on a fiber mount which is alignable in six-degrees of freedom. This helps to bring the crystal to the right position with the surfaces perpendicular to the incoming beams. Because the crystal is held by two clamps partially covering the crystal, $W_y = 7.4\,\mathrm{mm}$ is used as the crystal height in the following.

Different laser output powers are employed during the measurements. The intensities of the reference beam I_R, the phase-conjugated reference beam I_{R^*}, and the signal beam I_S right before the spatial frequency filter, component (3) in Fig. 4.11, are summarized for different nominal laser output powers P_L in Table 4.1. From this and specifications of the microscope objective we calculate for the peak intensity in the focus of the microscope

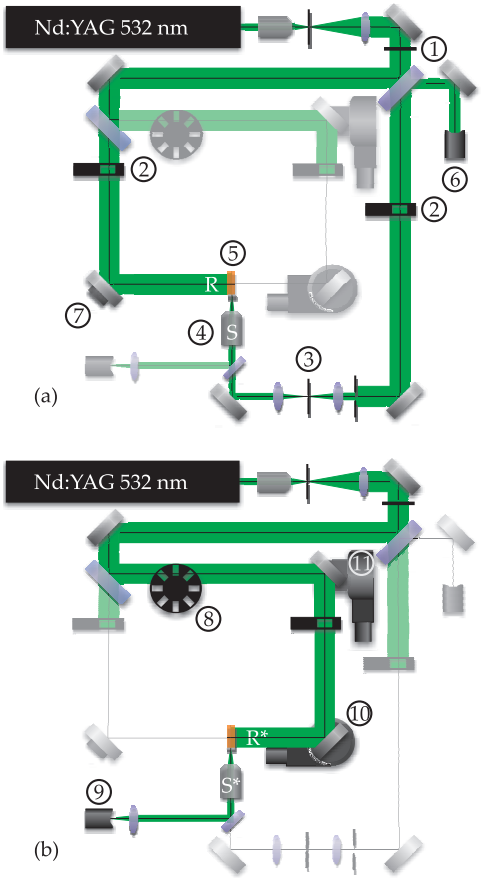

Figure 4.11: The experimental setup (a) during recording and (b) during read-out of a hologram. The numbers and details are explained in the text.

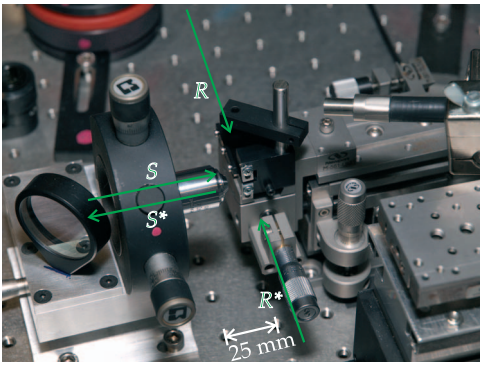

Figure 4.12: Photo of the crystal mount. The crystal is clamped between the two aluminum brackets in the center. The involved light beams S, R, R^*, and S^* are shown. (Photo: Tobias Beckmann)

objective $I_{S,\mathrm{in}} = 2.4 \times 10^8\,\mathrm{mW\,cm^{-2}}$.

P_L [W]	I_R [mW cm^{-2}]	I_{R^*} [mW cm^{-2}]	I_S [mW cm^{-2}]
1.0	107	61	96
0.5	52.1	29.9	48.9
0.1	8.7	5.0	8.1
0.01	0.61	0.35	0.55

Table 4.1: Laser light intensities in the experimental setup for different nominal laser output powers P_L.

Active stabilization

The recording times in iron-doped lithium niobate crystals can be one hour or more because of the small intensity of the signal wave behind the hole. During this time span, the relative phase between the signal beam S and the reference beam R has to be stable. Thus, the position of all components involved should be stable to a small fraction of the wavelength.

To eliminate vibrations caused by air movement, the whole setup is placed in a large box. But due to thermal drift, the required stability can

hardly be reached by passive means only. Thus, the relative phase is actively stabilized: S and R hit the crystal surface and the metal surface, and part of this light is reflected and guided back to the first beam splitter in the setup where the back-reflected beams are combined. The intensity at one point of the created stabilization interference pattern is recorded with a photodiode. If the pathlength of one of the two beams changes, the interference patterns changes, too. One mirror in the reference arm is placed on a piezo-mechanical translator. The mirror position is changed with a small periodic modulation. The corresponding change in the interference pattern is detected with a lock in-amplifier. This error signal is now fed to an integrator which controls the piezo-mechanical translator. Taken together, this stabilizes the holographic setup [79].

The reference and the signal wave propagate along their way twice: forward and backward. Thus, the relative phase change due to a distortion is twice as high as the distortion itself. Therefore, a distortion of $\lambda_0/2$ can not be detected by the stabilization system. Seldom, meaning once in several hours, sudden changes of the relative phase occur, which are faster than the stabilization system. In these cases, the system might stabilize to a relative phase shifted by π to the previous one and the previously recorded hologram is destroyed. Fortunately, these incidents are easy to detect because the integrated error signal, which is recorded, shows a sudden change in those cases. The stabilization system ensures that the signal fed to the piezomechanical translator stays in a previously determined window. When the signal reaches the upper boundary of the window, it is set to the lower boundary. Thus to minimize the number of sudden phase changes of π, the window size is chosen so that the relative phase of the reference and the signal beam changes as a multiple of 2π when the integrated error reaches the boundary.

4.2.3 Measurement procedure

First, the correct hole has to be found. The crystal can be moved and rotated with its mount. When the signal beam is switched on, the back-reflected light can be imaged on a CCD camera. With the microscope objective the double-structure in Fig. 4.7 is identifiable. After moving the crystal approximately to the next smaller hole we try to record a hologram. Usually the hole is not in the field of view of the microscope objective and several attempts to record a hologram have to be made. The smallest hole found by this method has a diameter of 150 nm.

After the crystal is aligned such that the stabilization system works and the microscope objective focuses on the correct sub-wavelength hole, a hologram is recorded for some minutes. For read-out the motorized rotation stages are used to align the read-out beam so that the diffracted light power is maximized. Afterwards all holograms are erased by illuminating the crystal for 15 min with incoherent light. A recording curve is taken by periodically reading out the hologram every 30 s. For this, the reference beam R is blocked for 3 s. At the same time, the phase-conjugated reference beam R^* illuminates the crystal. During read-out, the phase-conjugated signal light S^* is recorded with photodiode (9) in Fig. 4.11. A lock-in amplifier locked to the frequency of the mechanical chopper (8) is used to determine the diffracted light power P_d.

We use the diffracted light power P_d to calculate the diffraction efficiency η, which we define in our special situation to be

$$\eta = P_\mathrm{d} / (I_{R^*} W_y W_z). \tag{4.25}$$

The detected power P_d might be smaller than the power right behind the hole, as the microscope objective might not collect all the light. In the literature, the diffraction efficiency is often determined by dividing the diffracted light by the sum of the transmitted and diffracted light power. The latter definition ensures that reflection at the crystal surfaces and absorption do not play a role, whereas with our definition these effects diminish the diffraction efficiency. However, the diffraction efficiency, as we define it, is useful for comparison with results from computer simulations. Furthermore, we do not have to measure simultaneously the transmitted light power.

After a hologram is generated, angular selectivity curves can be recorded. This is done by detuning the read-out beam either in the plane of the table or perpendicularly to it. During detuning the diffraction efficiency is measured. Angular selectivity curves are taken at a laser output power of $P_\mathrm{L} = 0.01$ W to minimize erasure of the hologram by the read-out light.

In order to scan the diffraction efficiency for light being diffracted at different positions in the lithium niobate crystal, a circular diaphragm with 500 μm diameter is put into the read-out beam, approximately 2 cm before the crystal. The diaphragm is mounted on a motorized translation stage movable in the two-directions perpendicular to the read-out beam. In this case, the area of the diaphragm $\pi(250\,\mu\mathrm{m})^2$ is used instead of the crystal surface area $W_y W_z$ to calculate the diffraction efficiency by Eq. (4.25).

4.3 Results

Now, the experimental results for holographic phase conjugation through a sub-wavelength hole are presented. First, as a reference for the diffraction efficiency, plane-wave gratings are recorded in iron-doped lithium niobate crystals without gold film. Second, tight focusing by phase-conjugation through a sub-wavelength hole is tested by imaging the reconstructed spot after removing the gold film. Third, the evolution of the diffraction efficiency for holography through a hole in a gold film is investigated and angular selectivity curves as well as two-dimensional scans of the diffraction efficiency are presented.

4.3.1 Plane-wave holography

A grating is recorded with two plane waves. For this, the microscope objective (4) and the spatial frequency filter (3) are removed from the signal beam in the setup in Fig. 4.11, and an iron-doped lithium niobate crystal without gold film is mounted in the crystal holder. First, the hologram is read out with the reference wave. The signal wave S is blocked, and the diffracted light power is measured. After starting the recording, the diffraction efficiency increases and saturates at 16 % after about half an hour. For phase-conjugated read-out the phase-conjugated reference beam is used as read-out beam, and the phase-conjugated signal beam is detected with photodiode (9) in Fig. 4.11. The evolution of the diffraction efficiency can be seen in Fig. 4.13. The evolution is similar to the evolution for direct read-out and saturates at about 3 %.

When turning the crystal around the x-, y- and z-axis for 180°, the saturation value of the diffraction efficiency differs by a factor of up to 6 for the different crystal orientations.

When the crystal is illuminated only with the plane reference wave, the transmitted light intensity drops and saturates at about 25 % of the original transmission after about half an hour. The saturation value depends on which surface faces the reference wave. As the transmitted intensity drops, stray light appears behind the crystal. This stray light is polarized along the z-axis. The original transmission can be restored by illumination with incoherent light.

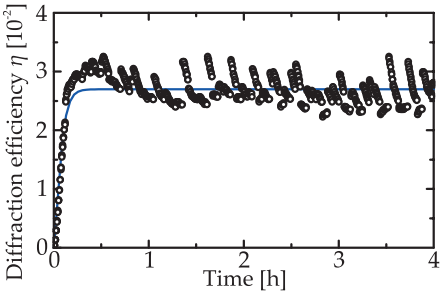

Figure 4.13: Evolution of the diffraction efficiency for a plane-wave grating. The hologram is read out with the phase-conjugated reference beam R^*. The laser output power is $P_L = 0.5\,W$. The solid line is a fit to a theoretical curve.

4.3.2 Tight focusing

Now we turn our attention to holographic phase-conjugation through a sub-wavelength hole. A crystal coated with a gold film with sub-wavelength holes is mounted in the crystal holder. The hologram is read-out with the phase-conjugated reference wave R^*. To image the reconstructed wave, we replace diode (9) in Fig. 4.11 by a CCD camera. The distance between the microscope objective and the crystal is changed until a sharp image is obtained on the camera. Figure 4.14 (a) shows the crystal surface when the phase-conjugated read-out beam is switched on, after a hologram is recorded through a hole with a diameter of 200 nm. The phase-conjugated light emerging from the sub-wavelength hole appears as a bright spot. Fitting a Gauss curve to the cross section in Fig. 4.14 (a), we find for the $1/e^2$-focus diameter $w_{S^*} = 1.2\,\mu$m.

To find out how good the focusing in the crystal works, we remove the metal film after recording a hologram. The crystal surface is depicted in Fig. 4.14 (b). The small, bright spot shows that the light is indeed focused. Fitting again a Gauss curve to the cross section, we find $w_{S^*} = 1.1\,\mu$m. The difference to the case with metal film is taken as the experimental error. The artifacts in both pictures are attributed to imperfections of the imaging system.

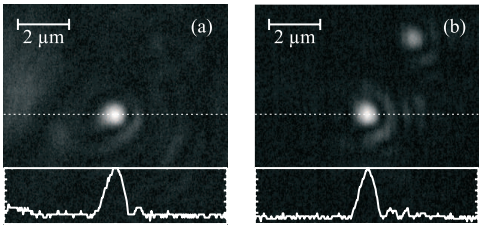

Figure 4.14: Phase-conjugated light (a) when the metal film is in place and (b) after the film is removed. Cross sections are added to measure the spot size. The hole diameter for this measurement is 200 nm.

4.3.3 Evolution of the diffraction efficiency

Now, we turn our attention towards quantitative measurements of the diffracted light power for holography through a sub-wavelength hole. This power is measured with photodiode (9) in Fig. 4.11, and the diffraction efficiency is calculated by Eq. (4.25). Figure 4.15 shows how the diffraction efficiency increases as we start recording, reaches a maximum and drops to a value close to zero afterwards. This is a completely different behavior compared with the evolution of the diffraction efficiency in the plane-wave case as seen in Fig. 4.13. Furthermore, for the 400-nm hole the diffraction efficiency is three orders of magnitudes smaller than for a plane wave grating. In all cases the recorded holograms can be erased with incoherent light. The phase-conjugated light S^* being back-transmitted through the hole, is polarized parallel to the y-axis. Thus, S and S^* have the same light polarization.

The evolution of the diffraction efficiency for three different hole sizes is shown in Fig. 4.16. The general behavior is very similar for all three curves. The diffraction efficiency increases, reaches a maximum, and drops to a value near zero. The smaller the hole size, the smaller gets the maximal diffraction efficiency. It is ten times smaller for the 500-nm hole and about thirty times smaller for the 400-nm hole compared to the 1000-nm hole. The time constants are identical for the three curves.

The measurements shown in Fig. 4.15 and Fig. 4.16 require active stabilization. If the stabilization system is turned off, the evolution of the diffraction efficiency becomes random and is not reproducible. Good re-

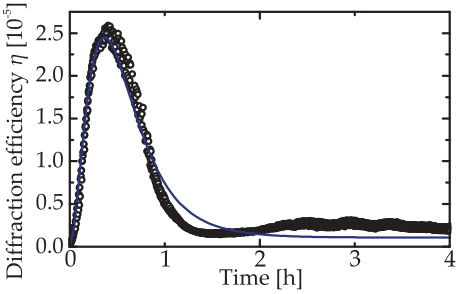

Figure 4.15: Evolution of the diffraction efficiency for a 400-nm hole. The laser output power is $P_L = 0.5\,W$. The solid line is a fit to a theoretical curve.

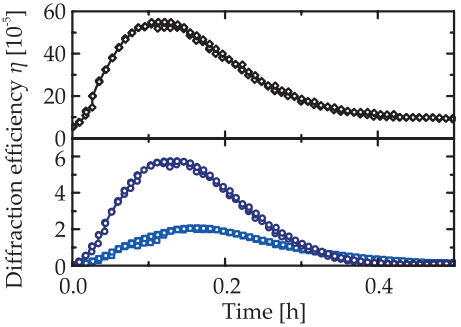

Figure 4.16: Evolution of the diffraction efficiency for holography with a 1000-nm hole (♢), a 500-nm hole (○), and a 400-nm hole (□). The laser output power is $P_L = 1\,W$.

producibility is found, when two measurements are taken without changing the setup in between: The error in the maximal diffraction efficiency is then smaller than 20 %. However, the reproducibility gets worse for longer recording times. For example, in Fig. 4.15 the diffraction efficiency increases a little bit between $t = 2\,\mathrm{h}$ and $t = 4\,\mathrm{h}$ before approaching the long-term saturation value. This is seen in some but not in all recording curves, and is therefore considered to be below the error. The reproducibility gets worse, if the setup is changed between two measurements. However, by optimizing all parameters an error smaller than 50 % can be reached.

4.3.4 Angular selectivity

The mirrors (10) and (11) in the experimental setup in Fig. 4.11 can be rotated so that the read-out beam is detuned in the x-z-plane (11), and in the y-z-plane (10). These mirrors are used to find the optimal diffraction efficiency during read-out. A hologram is recorded until the diffraction efficiency reaches its maximal value. Then, the read-out beam is detuned from the optimal value to obtain angular selectivity curves in the plane of the optical table and perpendicularly to it. Figure 4.17 (a) and (b) show the angular selectivity of two holograms: (a) For a 400-nm hole and (b) for a 1000-nm hole. Whereas the angular selectivity in the x-z-plane gets sharper for a bigger hole size, it decreases in the x-y-plane.

The angular selectivity in the x-y-plane for holography through a subwavelength hole is compared to those of a plane-wave grating and of a hologram written by a signal wave focused by a $\mathrm{NA} = 0.65$ microscope objective. For plane waves the diffraction efficiency is constant in the x-y-plane. For the case with the microscope objective the full width at half maximum of the selectivity curve is $0.24\,^\circ$. For a 400-nm hole it is $0.024\,^\circ$. The different curves are shown in Fig. 4.18. The diffraction efficiency is normalized to the maximal diffraction efficiency for each curve. The maximal diffraction efficiency for the plane wave is 2.7×10^{-2}, for the focused wave it is 2.1×10^{-3}, and for the hole it is 3.3×10^{-5}.

4.3.5 Razor-blade method

For the next measurements a two-dimensional translation stage is used to place either a razor blade or a circular diaphragm in the read-out beam.

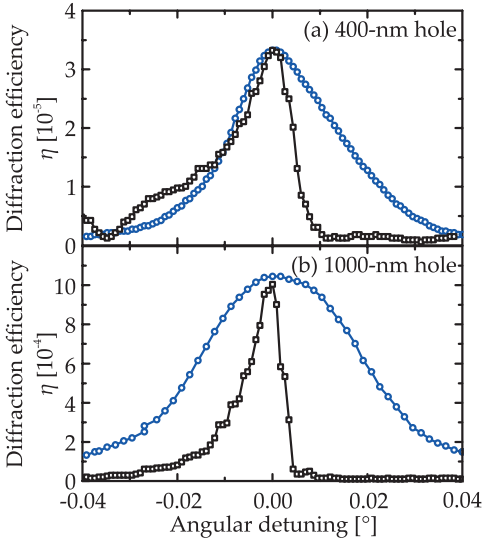

Figure 4.17: Angular selectivity curves for (a) a 400-nm and (b) a 1000-nm hole. Angular detuning is measured inside the crystal. □/○: rotations in the x-z/x-y-plane.

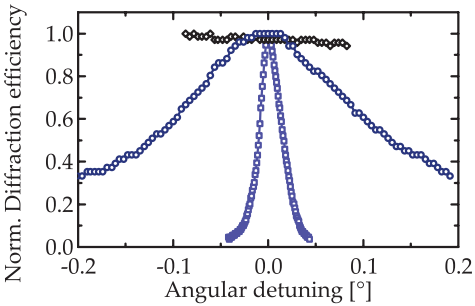

Figure 4.18: Angular selectivity in the x-y-plane for holography with a plane signal wave (♢), a signal wave focused with a NA $= 0.65$ microscope objective (○), and a signal wave transmitted through a 400-nm hole (□). The diffraction efficiency for each curve is normalized to the maximum. Angular detuning is measured inside the crystal.

Thus, the crystal is only partially illuminated, and the selected area of illumination is changeable via the translation stage. When calculating the diffraction efficiency, only the illuminated area of the crystal is taken into account. For a 500-μm diaphragm it is, for example, $P_{R^*} = \pi(250\,\mu\text{m})^2 I_{\text{in}}$. Because of the smaller area, the impinging light power decreases and the diffraction efficiency according to Eq. (4.25) can even be bigger than in the case of a completely illuminated crystal.

In a first step, a hologram is recorded through a 1000-nm hole until the maximal value is reached. During readout the razor blade is moved along the y-axis and afterwards along the z-axis. For movement in the z-direction, the crystal surfaces are approximately located at $z = 0\,\text{mm}$ and $z = 4\,\text{mm}$. For measurement in the y-direction the upper crystal border is approximately at $y = 4\,\text{mm}$. The accuracy of these positions is several hundred μm. The sub-wavelength hole is found on the z-surface at $z = 0\,\text{mm}$, $y = 1.5\,\text{mm}$. Figure 4.19 shows the diffraction efficiency as the crystal is revealed to the read-out light. In both directions the diffraction efficiency increases as more and more light impinges on the surface, reaches a maximum and drops afterwards. In the y-direction the diffraction efficiency changes very abruptly.

A circular 500-μm diaphragm is used in Fig. 4.20, where a two-dimen-

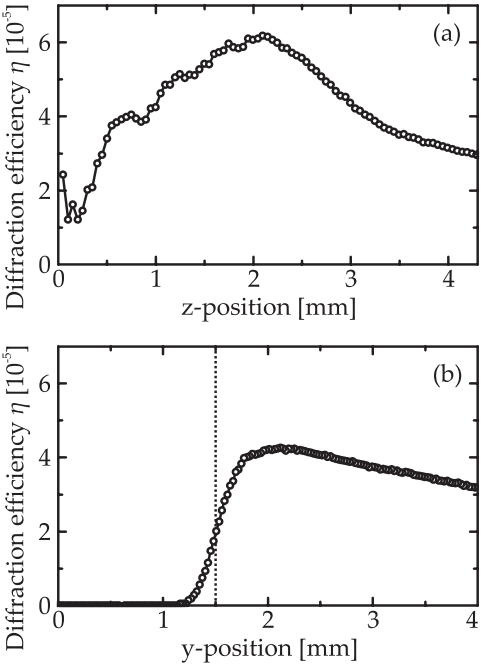

Figure 4.19: Diffraction efficiency versus the position of a razor blade for holography through a 400-nm hole. (a) The blade is moved along the z-axis. The sub-wavelength hole is approximately at the $z = 0$ position. (b) The blade is moved along the y-axis. The sub-wavelength hole is approximately at the $y = 1.5\,\mathrm{mm}$ position.

sional scan of the diffraction efficiency is shown. A maximum of the diffraction efficiency is found at the center of the picture. The peak has a full width at half maximum of about 400 μm in z-direction and of about 600 μm in the y-direction.

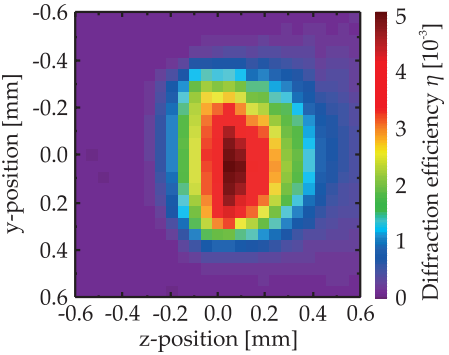

Figure 4.20: Two-dimensional scan of the diffraction efficiency of a hologram recorded with a signal wave through a 1000-nm hole.

Now, we study the position dependent evolution of the diffraction efficiency. After recording a hologram, the circular 500-μm diaphragm is placed in the read-out beam at the position, where the diffraction efficiency becomes maximal. Now, curves of η versus time are recorded with a laser power of $P_\mathrm{L} = 1\,\mathrm{W}$. Additionally, before each measurement, the crystal is illuminated with the reference beam R for different pre-illumination times t_p. Figure 4.21 (a) shows the resulting curves. A similar measurement is made after the diaphragm is moved 1.5 mm along the z-axis. The results can be found in Fig. 4.21 (b).

All curves in Fig. 4.21 increase, reach a maximum and saturate at a lower value. The time constant is approximately the same for all curves. The maximal diffraction efficiency for zero pre-illumination time drops by two orders of magnitude as the read-out position is moved. In Fig. 4.21 (a) the long-term saturation value is higher compared to that in Fig. 4.21 (b), where the saturation value is zero within the experimental error. With increasing pre-illumination time t_p, the maximal diffraction efficiency decreases. Different pre-exposure times for the signal beam S reveal no in-

fluence on the subsequent recording.

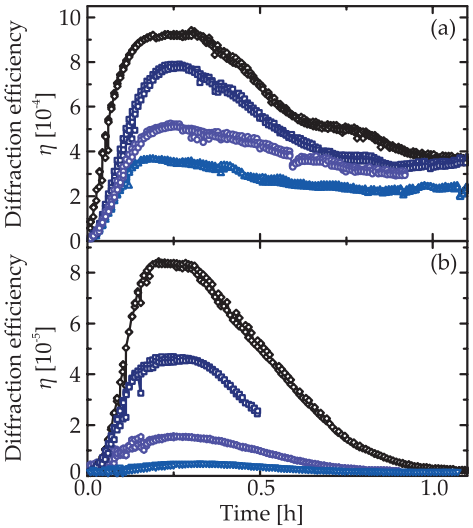

Figure 4.21: Evolution of the diffraction efficiency for a 1000-nm hole. A 500-μm diaphragm is placed in the read-out beam. The laser output power is $P_L = 1.0\,W$. The diaphragm is centered (a) at the position of maximal diffraction efficiency and (b) 1.5 mm along the z-direction away from the hole. Before recording, the crystal is pre-illuminated with the reference beam. Pre-illumination times – from top to bottom: (a) $t_p = 5.25, 30, 45, 150$ min and (b) $t_p = 0, 3.25, 5, 15$ min.

Angular selectivity curves are made at different positions of the diaphragm. It is found that the angle of maximal diffraction efficiency differs by up to 0.02°.

4.3.6 Summary of the experimental results

Looking at the experiments about holographic phase-conjugation through a sub-wavelength hole, we find that it works and light is nicely focused

by this method (Fig. 4.14). Reproducible curves of the diffraction efficiency versus time are recorded. The evolution is peculiar for holography through holes as the diffraction efficiency has a maximum after about half an hour (Fig. 4.15). The maximal diffraction efficiency decreases with the hole size (Fig. 4.16). For a 400-nm hole the efficiency is three orders of magnitudes smaller than for plane-wave gratings (compare Fig. 4.15 and Fig. 4.13). For holography through holes very sharp angular selectivity in two directions is found. The selectivity in the x-y-plane is more pronounced for smaller hole sizes (Fig. 4.17). For plane waves and for a focused signal wave without a hole the selectivity in the x-y-plane is far less pronounced (Fig. 4.18). Additional information is gained by using a translation stage to move a razor blade or a circular diaphragm in the read-out beam. It is found that most of the diffraction comes from areas close to the hole (Fig. 4.19 and Fig. 4.20). The temporal evolution of the diffraction efficiency is different for different places in the crystal. Closer to the hole the long term saturation value is much higher than far away from it (Fig. 4.21). If the crystal is illuminated with the reference beam prior to recording a hologram the maximal diffraction efficiency decreases (Fig. 4.21).

4.4 Discussion

The experimental data shows that holography through a sub-wavelength hole works and shows a very peculiar behavior compared to plane-wave gratings. In this section we want to understand these peculiarities. Furthermore, we discuss how the parameters can be further optimized. To understand the temporal evolution an analogy to the case of holograms written with two focused beams is drawn. The basic idea behind the further discussion is that a hologram is recorded by a spherical wave and a plane wave. To obtain the strength of the gratings inside the crystal, the formula in the sections 4.1.1 and 4.1.2 are evaluated. Then, the experiments are simulated using the scalar first-order Born approximation Eq. (4.23).

4.4.1 Diffraction efficiency in the plane-wave case

A diffraction efficiency of up to 16 % is measured for plane-wave recording and read-out with the original reference wave. Neglecting absorption and

reflection at the crystal surfaces, we can estimate the expected diffraction efficiency for the plane-wave case from [69]: $\eta = 1 - J_0^2(2\kappa\sqrt{W_x W_z}) - J_1^2(2\kappa\sqrt{W_x W_z})$, where J_0 and J_1 are Bessel functions of the first kind, $\kappa = (1/4)(2\pi n/\lambda_0)(\Delta\epsilon/\epsilon^{(0)})$, and n is the refractive index. The grating vector is tilted by 45° to the z-axis. Thus neglecting diffusion, and using literature values from [80] and [63], the electric space-charge field can be found from Eq. (4.12) $\Delta E_{SC} = \cos(45°)\beta_{322}/\sigma_{22} = 7.0\,\mathrm{MV\,m^{-1}}$. The effective $\Delta\epsilon$ can be calculated as $\Delta\epsilon = \cos(45°)(\epsilon^{(0)})^2 r_{322}\Delta E_{SC} = 1.2 \times 10^{-3}$. The crystal size is $W_x \times W_z = 1\,\mathrm{mm} \times 4\,\mathrm{mm}$. Thus, we get $\eta = 90\,\%$. Taking an absorption coefficient $\alpha = 560\,\mathrm{m^{-1}}$ into account, we get $\eta = 37\,\%$. At each crystal surface we loose about 15 % by reflection. Due to this reflected light the degree of modulation is at best $m_g = 0.8$. Thus we expect a diffraction efficiency of 26 %. The measured diffraction efficiency is 16 %.

We have seen that the transmitted light drops significantly, which is probably originating from holographic scattering. Since this scattering is caused by surface imperfections and since the experimentally observed drop of the transmitted light depends strongly on the surface through which the light enters the crystal, this is very plausible. Holographically scattered light decreases the degree of modulation of the interference pattern, therefore, this effect can contribute to the reduced diffraction efficiency.

Only $\eta = 3\,\%$ are measured when the crystal is read-out with the phase-conjugated reference beam. This is probably due to non-planar crystal surfaces. Thus, directing a plane wave onto the crystal with the direction opposite to the original reference wave does not generate the perfect R^* inside the crystal, and hence the diffraction efficiency gets smaller. The topographies of the crystal surfaces are shown in Fig. 4.5. Wedge-shaped deformations of the crystal surface can be compensated by tilting the phase-conjugated reference beam. But, since the crystal surface has a more complex shape, imperfections of the surface profile can not be compensated completely. Indeed, we see that slopes of 10^{-3} can be found. By refraction at the crystal surfaces a light beam thus can be distorted by 0.03° which is even more than the angular selectivity of 0.01°. Thus, it is understandable that due to non-perfect crystal surfaces the diffraction efficiency drops significantly.

In conclusion, by a better polishing of the surfaces, anti-reflection coatings and oxidized crystals, which absorb less, it should be possible to reach a diffraction efficiency close to 100 %.

4.4.2 Dynamics of the recording

As we have seen in section 4.1.1, for plane waves the amplitude of the dielectric constant modulation is expected to increase exponentially and then to saturate at $\Delta\epsilon_{\text{eff}}$ with a time constant $\tau = \epsilon\epsilon_0/(\sigma I^{(0)})$. The diffraction efficiency η, for $\eta \ll 1$, is expected to be $\eta \propto (\Delta\epsilon_{\text{eff}})^2$. This behavior is experimentally verified for a plane wave in Fig. 4.13. A fit of the theoretical curve is plotted as a solid line. The evolution of η for a 400-nm hole in Fig. 4.15 is different: In the beginning, the diffraction efficiency increases, but after about 0.5 h a maximum is reached and η decreases until it becomes close to zero after 1.5 h. In Fig. 4.21 (a) and Fig. 4.21 (b) the time constant is approximately half as high, which is expected, as the laser power used is twice as high.

Comparing the time constants in Fig. 4.21 (a) and Fig. 4.21 (b) we see that at both crystal positions the time constant is approximately the same. Thus the average light intensity has to be approximately the same. Since the intensity of the signal beam is strongly inhomogeneous, we conclude that the reference beam has a much bigger light intensity and thus is responsible for the speed of recording.

A possible explanation of the recording curve for the sub-wavelength hole is a field compensating the bulk photovoltaic driving force if the crystal is not illuminated completely [81]. If, for example, shadowing occurs at the crystal edges, the crystal would not be short-circuited and such a field would build up. Since after a long time the compensation field exactly counterbalances the bulk photovoltaic driving force, the remaining diffraction efficiency should originate only from the uncompensated parts of the driving force and be much smaller than the maximal value. The solid line in Fig. 4.15 indicates a fit of $P_1\{t\exp(-t/\tau) + P_2[1-\exp(-t/\tau)]\}^2$, with P_1, P_2, τ being fit parameters. This curve describes the expected evolution if the compensation effect occurs [81].

The interpretation that a compensation effect is responsible for the decreasing diffraction efficiency, is also supported by the pre-illumination data in Fig. 4.21 (a) and Figs. 4.21 (b): With increasing pre-illumination time t_{p}, the maximum of the diffraction efficiency decreases, because already part of the compensating field has built-up. The fact that pre-illumination with the signal beam has no effect, can be understood: The reference beam R is brighter than the signal wave S in most parts of the crystal and, furthermore, it is the reference beam which is partially shadowed.

Shadowing at the borders might be responsible for the incomplete il-

lumination: all four surfaces not exposed to the reference beam are coated with an optically thick material. If the crystal is not aligned completely parallel to the reference beam or if the surface is shaped slightly convex, shadowing can occur at the crystal border. This is shown in Fig. 4.22.

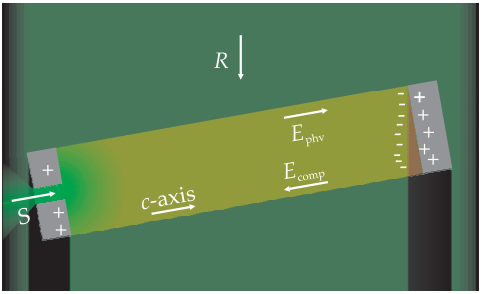

Figure 4.22: Illustration of inhomogeneous illumination of the lithium niobate crystal: Due to shadowing a compensation field may build up, which counterbalances the bulk photovoltaic effect.

Another issue concerning the dynamics is that the time constant of holographic recording depends on the light intensity, but in our geometry the intensity varies through the crystal. If the crystal width is $W_x = 1\,\mathrm{mm}$, the factor between the light intensity of the reference beam R in the front of the crystal and at the back-side will be $\exp(-\alpha W_x) = 0.57$. The time constant τ is different by this factor. Close to the hole very small time constants might occur, as the signal beam is brighter there and can increase the average light intensity. Furthermore, the speed of the local grating build-up does not only depend on the local light intensity $I^{(0)}$, but also on the grating orientation. According to [63], the effective dielectric constant is $\epsilon_{\mathrm{eff}}^{\mathrm{static}} \approx 90$, if the grating vector $\boldsymbol{K}_{\mathbf{g}}$ is parallel to the x- or the y-axis, and $\epsilon_{\mathrm{eff}}^{\mathrm{static}} \approx 30$, if it is parallel to the z-axis. This implies that even for the same light intensity time constants being different by a factor of three can occur in the lithium niobate crystal.

4.4.3 Holography of a point source

The model

In the following, we model the hologram in the crystal to interpret our experimental data. The situation is shown in Fig. 4.23. The spherical signal wave S and the plane reference wave R record a hologram. The hologram can be described by local grating vectors $\boldsymbol{K_g}(\boldsymbol{r})$. When the hologram is read-out with the plane read-out wave, which is close to the phase-conjugated reference wave R^*, the phase-conjugated signal wave S^* is reconstructed. The focus of the spherical wave is located at $\boldsymbol{r} = 0$, the crystal is found in the $r_z > 0$ space. The reference wave is aligned anti-parallel to the x-direction. For the cause of simplicity we assume that the crystal has an isotropic index of refraction of $n = [\epsilon^{(0)}]^{0.5} = 2.3$.

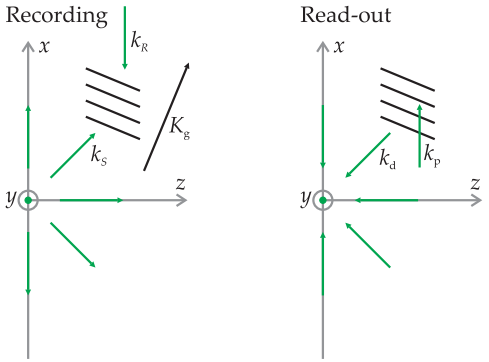

Figure 4.23: Scheme of holographic phase conjugation of a point source. The propagation vectors of the signal wave $\boldsymbol{k_S}$, the reference wave $\boldsymbol{k_R}$, the read-out wave $\boldsymbol{k_p}$, and the diffracted wave $\boldsymbol{k_d}$ are shown. Furthermore, the grating with vector $\boldsymbol{K_g}$ is shown at one position.

As it is pointed out in Chapter 2, neither theoretical nor experimental data is available to accurately describe transmission characteristics of subwavelength holes in real metals. According to [7], we approximate the signal wave by a magnetic dipole field, where the magnetic dipole $\boldsymbol{M}$ is perpendicular to the incoming electric field vector $\boldsymbol{A_{in}}$. The electric field is then $\boldsymbol{A_S} \propto (\boldsymbol{k_S} \times \boldsymbol{M}) \exp(ik|\boldsymbol{r}|)/|\boldsymbol{r}|$, where $|\boldsymbol{r}|$ is the distance to the hole,

and $k = 2\pi n/\lambda_0$.

In the experiments, the hole diameters $2r_\mathrm{h}$ are comparable to the wavelength. Thus, the signal wave is expected to diffract less, and a dipole approximation is no longer appropriate. To model this, we use Kirchhoff's scalar diffraction theory, which is applicable for hole diameters larger than the wavelength [12]. We use the fact that the hole is illuminated with a plane wave with field amplitude A_in. As an approximation, $\exp(ik|\boldsymbol{r}-\boldsymbol{r'}|)/|\boldsymbol{r}-\boldsymbol{r'}| \approx \exp(ik|\boldsymbol{r}|)/|\boldsymbol{r}|\exp(ikr'_l r_l/|\boldsymbol{r}|)$ holds for points $\boldsymbol{r'}$ in the area of the hole S_h with $|\boldsymbol{r'}| < |\boldsymbol{r}|$ [12]. We get for the signal wave amplitude A_S [12]:

$$\begin{aligned} A_S(\boldsymbol{r}) &= -\frac{i}{2\lambda}A_\mathrm{in}\int_{S_\mathrm{h}} \mathrm{d}S_\mathrm{h}(\boldsymbol{r'})\frac{\mathrm{e}^{ik|\boldsymbol{r}-\boldsymbol{r'}|}}{|\boldsymbol{r}-\boldsymbol{r'}|}\left[1+\cos(\phi)\right] \\ &= -\frac{i}{2\lambda}A_\mathrm{in}\frac{\mathrm{e}^{ik|\boldsymbol{r}|}}{|\boldsymbol{r}|}\left[1+\cos(\phi)\right]\int_{S_\mathrm{h}} \mathrm{d}S_\mathrm{h}(\boldsymbol{r'})\mathrm{e}^{ikr'_l r_l/|\boldsymbol{r}|}, \end{aligned} \tag{4.26}$$

where ϕ is the angle between $\boldsymbol{r}$ and the z-axis. The integral is the same which occurs in calculating the Fraunhofer diffraction of a circular opening and we obtain for the diffracted signal wave:

$$A_S(\boldsymbol{r}) = -\frac{i}{\lambda}A_\mathrm{in}\frac{\mathrm{e}^{ik|\boldsymbol{r}|}}{|\boldsymbol{r}|}\frac{1}{2}\left[1+\cos(\phi)\right]\,\pi r_\mathrm{h}^2\, 2\frac{\mathrm{J}_1[kr_\mathrm{h}\sin(\phi)]}{kr_\mathrm{h}\sin(\phi)}. \tag{4.27}$$

Additionally, we use the magnetic dipole polarizations as predicted by Bethe. Hence, the signal wave is a spherical wave, where the angular distribution is modulated according to an Airy disc and a $0.5[1+\cos(\phi)]$ factor. But we still use a scalar calculation and even for a vectorial calculation we would have incorrect boundary conditions as Bethe pointed out [7]. Thus, for very small hole diameters our approximation is expected to fail. Nevertheless, we use Eq. (4.27) to model the signal wave for holes with $r_h \geq 200\,\mathrm{nm}$.

As we have seen, the saturation space-charge field depends on the degree of modulation m_g of the interference pattern and thus only on the relative intensity of the reference wave R and the signal wave S. At some point along the z-axis $r_x = r_y = 0$ and $r_z = r_\mathrm{e}$ the intensities of the signal wave and the reference wave are equal. We incorporate absorption, assume for the reference wave $|A_R(\boldsymbol{r})|^2 = \exp(\alpha r_x)$ and rewrite the amplitude of the signal wave in terms of the radius of equal intensity r_e:

$$|A_S(\boldsymbol{r})| = |A_\mathrm{in}|\frac{r_\mathrm{e}\mathrm{e}^{-(\alpha/2)|\boldsymbol{r}|}}{|\boldsymbol{r}|\mathrm{e}^{-(\alpha/2)r_\mathrm{e}}}\frac{1}{2}\left[1+\cos(\phi)\right]\,2\frac{\mathrm{J}_1[kr_\mathrm{h}\sin(\phi)]}{kr_\mathrm{h}\sin(\phi)}. \tag{4.28}$$

The strength of the recorded index-of-refraction grating strongly depends on the grating vector direction and the involved light polarizations. We soon use our model signal wave $\boldsymbol{A_S}$ and reference waves $\boldsymbol{A_R}$ to evaluate the formula provided in sections 4.1.1 and 4.1.2. Therefore, we have then a complete description of the hologram recorded by a plane wave and a wave transmitted through a sub-wavelength hole. And this description depends on just one free parameter: The radius of equal intensity r_e.

The light intensity of the signal beam just before the sub-wavelength hole is supposed to be $I_\mathrm{in} = 2.4 \times 10^9\,\mathrm{W\,m^{-2}}$. Using Eq. (4.27) and taking absorption into account, the radius of equal intensity for different hole diameters can be calculated. We find $r_\mathrm{e} = 0.76\,\mathrm{mm}$ for a 400-nm hole, $r_\mathrm{e} = 1.1\,\mathrm{mm}$ for a 500-nm hole, and $r_\mathrm{e} = 2.7\,\mathrm{mm}$ for a 1000-nm hole. However, we find much better agreement between theoretical and experimental data for smaller r_e. This could be due to a transmission efficiency T_h of the hole being smaller than one. Thus, we take r_e as a fit parameter, and in the following we use $r_\mathrm{e} = 0.2\,\mathrm{mm}$ for a 400-nm hole and calculate for the other holes, assuming that the input intensity is the same: $r_\mathrm{e} = 0.3\,\mathrm{mm}$ for a 500-nm hole, and $r_\mathrm{e} = 1.0\,\mathrm{mm}$ for a 1000-nm hole.

Now, since we have a complete description of the hologram, we calculate diffraction by this hologram. For this, we assume that a scalar approximation can be used and the diffraction efficiency is small. Hence, we simplify the Born approximation Eq. (4.23). We are only interested in points $\boldsymbol{r}$ around $\boldsymbol{r} = 0$. Thus we can assume $|\boldsymbol{r}| \ll |\boldsymbol{r'}|$ for most points $\boldsymbol{r'}$ in the crystal, and we can again use the approximation [12]: $\exp(ik|\boldsymbol{r} - \boldsymbol{r'}|)/|\boldsymbol{r} - \boldsymbol{r'}| \approx [\exp(ik|\boldsymbol{r'}|)/|\boldsymbol{r'}|]\exp(-ikr_l r'_l/|\boldsymbol{r'}|)$. If the dielectric constant changes proportional to the interference pattern of the plane reference wave and a spherical signal wave, we can write:

$$\epsilon^{(1)}(\boldsymbol{r'}) = c(\boldsymbol{r'})\mathrm{e}^{-ik|\boldsymbol{r'}|}\mathrm{e}^{ik_{R,l}r'_l}, \tag{4.29}$$

where $c(\boldsymbol{r'})$ is a function which varies on much larger scales than the wavelength of light.

We assume that the the hologram is illuminated with a plane read-out wave $A_\mathrm{p}(\boldsymbol{r'}) = \tilde{A}_\mathrm{p}(\boldsymbol{r'})\exp(ik_{\mathrm{p},l}r'_l)$. Inserting this in the Born approximation Eq. (4.23), we get:

$$A_\mathrm{d}(\boldsymbol{r}) = \left(\frac{2\pi}{\lambda_0}\right)^2 \int \mathrm{d}^3\boldsymbol{r'} \frac{c(\boldsymbol{r'})\tilde{A}_\mathrm{p}(\boldsymbol{r'})\mathrm{e}^{-(\alpha/2)|r|}}{r'} \mathrm{e}^{-ikr_l r'_l/|\boldsymbol{r'}|}\mathrm{e}^{ir'_l(k_{\mathrm{R},l}+k_{\mathrm{p},l})} \tag{4.30}$$

for the diffracted wave. For known $c(\boldsymbol{r'})$ and $\tilde{A}_\mathrm{p}(\boldsymbol{r'})$ this integral can be

numerically evaluated as the arguments of the exponential functions vary slowly for small $|\boldsymbol{r}|$ and for small detuning $|\boldsymbol{k}_\mathbf{R} + \boldsymbol{k}_\mathbf{p}|$.

In this model, the diffraction efficiency is calculated by determining the diffracted field $A_\mathrm{d}(0)$ at $\boldsymbol{r} = 0$. Thus the diffraction efficiency is:

$$\eta = \frac{\pi r_\mathrm{h}^2 |A_\mathrm{d}(0)|^2}{(|A_\mathrm{p}(r_x = -W_x/2)|^2 W_y W_z}. \tag{4.31}$$

This definition of the diffraction efficiency is consistent with the experimentally defined value as long as the intensity of the diffracted light does not vary considerably over the area of the hole. Thus, it is consistent for small holes. Otherwise, an integration over the area of the hole would be necessary.

Focus width

Now, we study the size of the reconstructed focus, depending on the form of the coupling constant inside the crystal. For this, we assume that we can neglect absorption and that we can write:

$$c(\boldsymbol{r'})\hat{A}_\mathrm{p}(\boldsymbol{r'}) = c_\mathrm{r}(r')c_\mathrm{S}(\phi). \tag{4.32}$$

Furthermore, we assume that $c_\mathrm{S}(\phi) = 1$ for $\pi/2 - \omega < \phi < \pi/2$ and $c_\mathrm{S}(\phi) = 0$ for $\phi < \pi/2 - \omega$. Thus ω is an opening angle of the hologram, and consequently we can define a numerical aperture of the hologram by $\mathrm{NA}_\mathrm{h} = n \sin\omega$. In analogy to the Airy-criterium for the resolution of a microscope objective, we can relate the focus size to the angle ω. We define:

$$\boldsymbol{s}(\theta, \phi) = \begin{pmatrix} \sin\theta \sin\phi \\ \cos\theta \sin\phi \\ \cos\phi \end{pmatrix}. \tag{4.33}$$

We calculate the diffracted light for Bragg-read-out. Thus we get:

$$\begin{aligned} A_\mathrm{d}(\boldsymbol{r}) = \left(\frac{2\pi}{\lambda_0}\right)^2 \int_0^R \mathrm{d}r' r' C_\mathrm{r}(r') \\ \times \int_{-\pi}^{\pi} \mathrm{d}\theta \int_0^{pi/2} \mathrm{d}\phi \cos(\phi) C_\mathrm{S}(\phi) \mathrm{e}^{-ikr_l s_l(\theta,\phi)}. \end{aligned} \tag{4.34}$$

Since the spot size is isotropic in the x-y-plane, we can assume: $r_y = |\boldsymbol{r}|$

and $r_x = r_z = 0$. Then we get:

$$\begin{aligned} A_{\mathrm{d}}(\boldsymbol{r}) &= \left(\frac{2\pi}{\lambda_0}\right)^2 \int_0^R \mathrm{d}r' r' C_{\mathrm{r}}(r') \\ &\quad \times \int_{-\pi}^{\pi} \mathrm{d}\theta \int_0^{pi/2} \mathrm{d}\phi \cos(\phi) C_{\mathrm{S}}(\phi) \mathrm{e}^{-ik|\boldsymbol{r}|\sin(\theta)\cos(\phi)} \\ &= -\frac{(2\pi)^3}{\lambda_0^2} \int_0^R \mathrm{d}r' r' C_{\mathrm{r}}(r') \int_0^{\omega} \mathrm{d}\phi' \sin(\phi') J_0(k|\boldsymbol{r}|\sin(\phi')) \end{aligned} \tag{4.35}$$

For $\omega \ll 1$ we can approximate $\sin(\phi') = \phi'$ and we retain the integral leading to an Airy-disk [12]. Thus, the position of the first zero of the diffracted field is

$$r_0 = 0.61 \frac{\lambda_0}{n \sin(\omega)}. \tag{4.36}$$

For larger ω we numerically evaluate the integral and get for $\omega \to \pi/2$:

$$r_0 = 0.50 \frac{\lambda_0}{n \sin(\omega)}. \tag{4.37}$$

Intermediate values of the factor in the front are found for ω between these extremes.

Now we analyze the experimental measurements of the focus size. The small spot in Fig. 4.14 (b) is the focused light, when the metal film is removed. Within the experimental errors, the focus width is not bigger than in the case, where the metal film is still in place and all the light emerges from the sub-wavelength hole (Fig. 4.14 (a)). The diameter of the $1/\mathrm{e}^2$-focus in both cases is about $(1.1 \pm 0.1)\,\mu$m. We approximate the image of a point source by a Gauss curve with width w_{ps} and the spot of the reconstructed beam by a Gauss curves with width w_{focu}. Then, the combined width w_{comb} is the width of the convolution of the two Gauss curves. Hence: $w_{\mathrm{comb}} = \sqrt{w_{\mathrm{ps}}^2 + w_{\mathrm{focu}}^2}$. We find that a focus size of $w_{\mathrm{focu}} = 0.5\,\mu$m is the largest compatible with the error margin. This corresponds to a full width at half maximum of the focused spot size of $0.3\,\mu$m. And by using Eq. (4.37) this corresponds to a numerical aperture of at least $\mathrm{NA_h} = 0.9$.

Grating strength

Due to the low symmetry of lithium niobate crystals, many material parameters show a strong orientation dependence. As we have seen in section 4.1.1 and in section 4.1.2 this is especially true for the photorefractive

effect. Therefore, the question arises, in which directions the crystal allows efficient recording of gratings. To investigate this question, the formula in the sections 4.1.1 and 4.1.2 are evaluated. For the material parameters literature values are used. The effective change of the dielectric tensor and the material parameters are found in [63]. The elements for the bulk photovoltaic tensor and the specific photoconductivity are taken from [82] and are scaled to the appropriate oxidization state $c_{\mathrm{Fe}^{2+}}/c_{\mathrm{Fe}^{3+}} = 0.09$ according to [80].

Fig. 4.24 shows the saturation space-charge field ΔE_{SC}, the effective electro-optic coefficient r_{eff}, and the effective change of the dielectric constant $\Delta\epsilon_{\mathrm{eff}}$. The situation shown in Fig. 4.23 is assumed, and the data is plotted versus the direction of the signal wave vector $\boldsymbol{k}_S$. To project the directions onto the screen, a Lambert azimuthal equal-area projection is used, and the z-axis is in the center of the figures. The colatitude ϕ is the angle to the z-axis and the longitude θ is measured to the y-axis.

First, we discuss the saturation space-charge field ΔE_{SC} shown in Fig. 4.24 (a). This field is mainly due to three contributions: The coefficient β_{322} of the bulk photovoltaic tensor, and, less important, the coefficients β_{223} and β_{232} and diffusion currents. The β_{322} coefficient is the only relevant contribution of the photovoltaic tensor in the x-z-plane, as all involved waves are polarized along y there. The resulting space-charge field becomes maximal, $\Delta E_{\mathrm{phv}} = \beta_{322}/\sigma_{22} = 9.9\,\mathrm{MV\,m^{-1}}$, in the negative x-direction as the grating vector is oriented closely along the z-direction, and it vanishes in the positive x-direction as the grating vector is close to the x-axis here. However, the magnitude of the grating vector is largest in the positive x-direction. This is why the diffusion field, which is proportional to the grating vector length, becomes maximal in this direction, reaching values of $\Delta E_{\mathrm{diff}} = i\frac{k_B T}{q_e}|\boldsymbol{K}_{\mathbf{g}}| \approx i\,1.4\,\mathrm{MV\,m^{-1}}$. The phase of the diffusion grating is shifted by 90° to the interference pattern. A shift also occurs for the third contribution, which comes from the β_{223} and β_{232} coefficients, thus, the signal and the reference waves have different polarization. This is the case for signal wave vectors close to the equator.

Figure 4.24 (b) shows the effective electro-optic coefficient. Again the situation is easier for signal wave vectors in the x-z-plane. In this plane, the tensor element is close to $r_{\mathrm{eff}} = \cos(\xi)\,9.1 \times 10^{-12}\,\mathrm{mV^{-1}}$ [63], with ξ being the angle between $\boldsymbol{K}_{\mathbf{g}}$ and the z-axis. A very large r_{eff} can be found close to the equator. This is due to the strong coefficient $r_{\mathrm{eff},23}$, which reaches $r_{\mathrm{eff},23} > 30 \times 10^{-12}\,\mathrm{mV^{-1}}$ for grating vectors in the x-y-

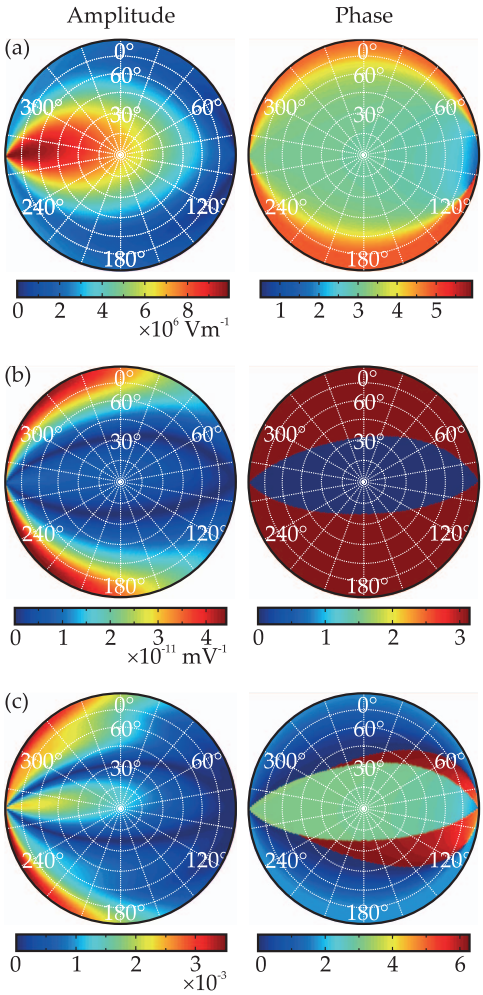

Figure 4.24: (a) The saturation space-charge field, (b) the effective electro-optic coefficient and (c) the effective dielectric constant change for different directions of the signal wave.

plane [63]. When the contributions from $r_{\text{eff},22}$ and from $r_{\text{eff},23}$ cancel each other, the effective electro-optic coefficient vanishes. This is why the pattern in Fig. 4.24 (b) is so narrow in the $\pm y$-direction.

When the space-charge field, the effective electro-optic tensor, and the factor $[e^{(0)}]^2$ are multiplied, the effective change of the dielectric constant $\Delta\epsilon_{\text{eff}}$ is found. This is shown in Fig. 4.24 (c). In the $\pm y$-direction the zero of the dielectric constant change is approximately at $\phi = 25°$. The central area with high diffraction efficiency is wider in the $\pm x$-direction, with a maximum close to the $-x$-direction.

Together with the model for the signal wave S in Eq. (4.28) for diffraction by holes with different diameters, we have a complete description of the degree of modulation in the crystal and can model the grating strength everywhere. In Fig. 4.25 amplitude and phase of the corresponding gratings $m_g\Delta\epsilon_{\text{eff}}$ in the y-z-plane are shown for a 400-nm hole and for a 1000-nm hole. Two distinct regions are found: First, a central region with constant phase, which corresponds to gratings recorded mainly by the β_{322} component of the bulk photovoltaic tensor. And a second region, where side-lobes occur. Because these side lobes are close to the x-y-plane, they are anisotropically recorded and, thus, the gratings are phase-shifted to the interference pattern.

According to the simulations in Fig. 4.25 a rather exotic effect can significantly contribute to holography through a sub-wavelength hole: Anisotropic recording from the side lobes of the signal wave. For comparison, we introduce an alternative model, where exotic recording does not occur: we assume a direction independent change of the dielectric constant $\Delta\epsilon_{\text{eff}}$, which shows a constant phase, and is geometrically truncated to the area which is illuminated by the zero-order light cone of the signal wave. This corresponds to the assumptions made for Eq. (4.32). We call this the simplified model. When used in the following, it is specially noted.

However, a first indication that exotic recording is relevant can be found in Fig. 4.21. In Fig. 4.21 (a) the measurements are made close to the hole. According to Fig. 4.25 areas with exotic recording are read out. Thus, even after the β_{322} component is counterbalanced by a compensation field the exotic parts of the hologram can diffract light and thus the long term saturation value of the diffraction efficiency is not zero. In Fig. 4.21 (b), where the hologram is read-out far away from the hole, only gratings recorded by the β_{322} element of the bulk photovoltaic tensor contribute. Due to the compensation of β_{322} the diffraction efficiency should go to zero, exactly what is measured.

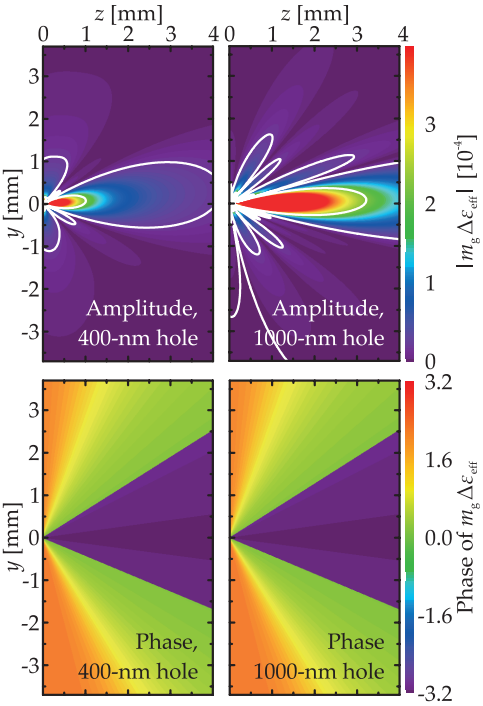

Figure 4.25: Amplitude and phase of the grating strength $m_g \Delta\epsilon_{eff}$ in the y-z-plane for a 400-nm hole and a 1000-nm hole. The amplitude is clipped at 4×10^{-4} to accentuate the side lobes. The maximal value in the plane shown is $|m_g \Delta\epsilon_{eff}| = 1.4 \times 10^{-3}$.

Angular selectivity

If the read-out beam impinging on a plane-wave grating in the x-z-plane is angularly detuned in the x-z-plane, the diffracted light shows a strong selectivity. But the diffraction efficiency shows nearly no selectivity if the read-out beam is detuned perpendicular to this plane. Figure 4.17 shows strong selectivity for detuning in both directions. This proves that a large fraction of the light has to be diffracted by gratings with grating vectors $\boldsymbol{K_g}$ which do not lie in the x-z-plane. The effect becomes more pronounced for smaller hole sizes as the signal light is diffracted stronger.

In Fig. 4.26 simulated angular selectivity curves for a 400-nm and a 1000-nm hole are shown. The width of the curves are slightly narrower compared to those of the measured data in Fig. 4.17. In both, in the experimental data and in the simulation, the selectivity in the x-z-plane is asymmetric. The effect is stronger for the 400-nm hole than for the 1000-nm hole. The direction of enlarged selectivity depends on the orientation of the crystal. By modifying the model we try to find the cause of this asymmetry. First, the angular selectivity curves are strictly symmetric if the simplified model is used. Second, no asymmetry is found if a constant complex phase for $\Delta\epsilon_{\text{eff}}$ is assumed. And third, no asymmetry is found if the signal wave is geometrically truncated outside a $\text{NA}_\text{h} = 2.0$ cone. Thus, whenever we exclude the exotic gratings, the asymmetry disappears. This is a second evidence that exotic gratings significantly contribute to the overall diffraction. If the radius of equal intensity r_e is further reduced, the amplitude but not the shape of the curves change. Whereas for an increase in r_e the asymmetry increases.

In Fig. 4.18 the angular selectivity in the vertical direction is compared for holography with a plane signal wave, a signal wave focused with a $\text{NA} = 0.65$ microscope objective, and a signal wave transmitted through a 400-nm hole. The nearly constant diffraction efficiency of the plane wave is understandable, and we already discussed the angular selectivity curves for the sub-wavelength hole. Surprising is the wide selectivity for the microscope objective. To simulate the case of the microscope objective, the simplified model for holography through a hole with four different numerical apertures is used: $\text{NA}_\text{h} = 0.25, 0.50, 0.75, 1.00$. The angular selectivity curves are shown in Fig. 4.27. The experimentally measured selectivity for the microscope objective is by far less pronounced than the simulated data even for $\text{NA}_\text{h} = 0.25$. Thus a low NA_h can hardly be the cause for the wide selectivity. A huge difference between the cases of hologra-

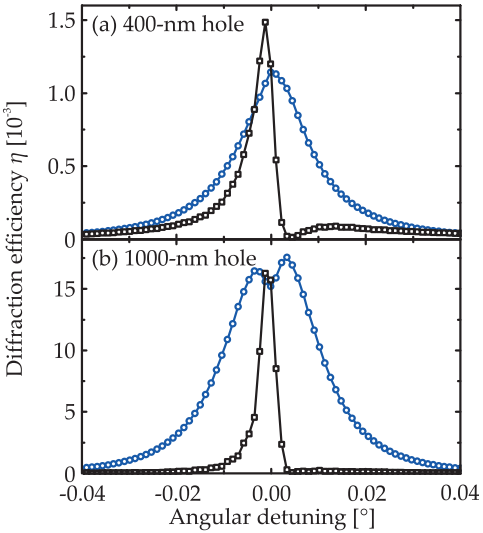

Figure 4.26: Simulated angular selectivity for (a) a 400-nm and (b) a 1000-nm hole. □/○: rotations in the x-z/x-y-plane.

phy through a hole in a metal film and holograph with a wave focused by a microscope objective is that in the case with the sub-wavelength hole only the light being focused onto the hole is measured. In the contrary, in the case with the microscope objective all the diffracted light can be measured even if the light is being focused on a different position. Indeed, simulations using the method in [72] indicate that if the read-out beam is detuned, the position of the reconstructed focus moves. Thus, the model, which calculates the diffracted intensity only at $\boldsymbol{r} = 0$, is not applicable. The sharp selectivity in the case with the sub-wavelength hole is due to the fact that the light is no longer being focused onto the hole. In fact, if we look upon Eq. (4.30), we see that the phase term for $\boldsymbol{r} \neq 0$ might partially compensate the phase term from detuning. Thus the focus might move for a detuned read-out wave, though the total amount of the diffracted light does not decrease as drastically.

Razor-blade measurements and two-dimensional scan

We use the model to calculate the diffraction efficiency η for a 400-nm hole when only parts of the crystal are illuminated with the read-out beam. Figure 4.28 shows the computed diffraction efficiency for a razor blade moved in the horizontal and in the vertical direction. Experimentally, the absolute position of the razor blade has an error of several hundred micrometer. This error strongly influences the amount of the impinging light and thus the diffraction efficiency. To simulate the influence of this uncertainty, curves with shifted razor blade positions are plotted for the horizontal movement simulations. Comparing the simulations with the experimental data in Fig. 4.19 we see the same behavior: In the horizontal direction the diffraction efficiency increases, reaches a maximum at approximately $z = 1.5\,\mathrm{mm}$ and drops to a lower value. In the vertical direction the diffraction efficiency begins to rise shortly before the hole is exposed and reaches a maximum after the razor blade is moved less than a millimeter further.

Using the simplified model, where the signal beam is truncated outside a certain cone, very similar curves as in Fig. 4.28 result, depending on the simulation parameters r_e and the numerical aperture $\mathrm{NA_h}$.

Furthermore, the model is used to simulate the two-dimensional scan of the diffraction efficiency for a 1000-nm hole with a 500-μm diaphragm. The result is shown in Fig. 4.29. Compared to the experimental data in Fig. 4.20 the simulated data is broader in the z-direction and narrower in

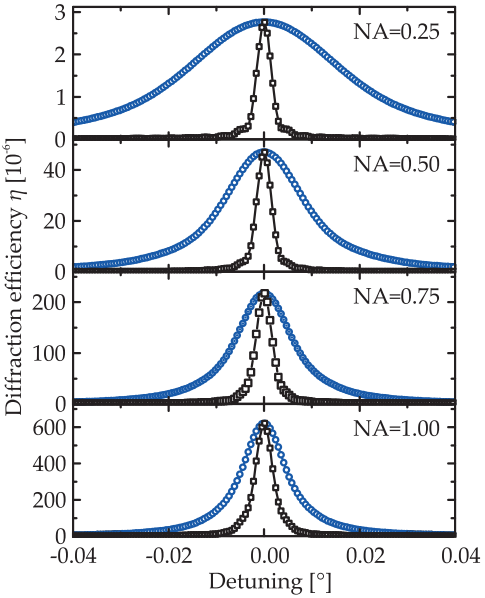

Figure 4.27: Simulated angular selectivity curves calculated with the simplified model for different numerical apertures of the hologram $NA_h = 0.25, 0.50, 0.75, 1.00$. □/○: rotations in the x-z/x-y-plane.

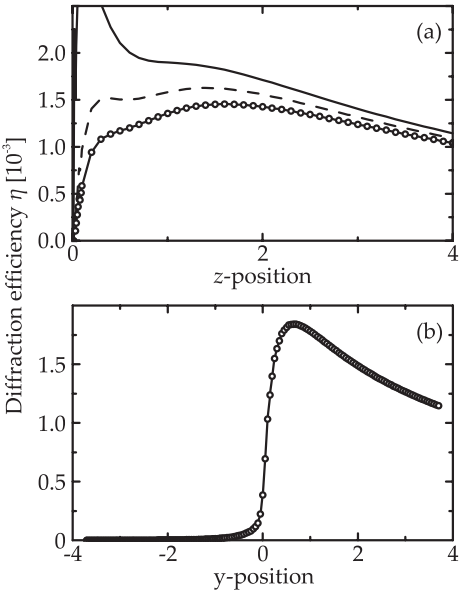

Figure 4.28: Simulated diffraction efficiency η versus the position of a razor blade (a) in the horizontal direction and (b) in the vertical direction. For the horizontal movement in (a) the zero-position of the blade is assumed to be shifted by 0 μm (solid line), 200 μm (dashed line), 400 μm (circles).

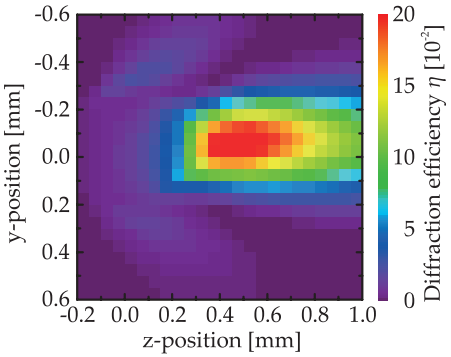

Figure 4.29: Computed two-dimensional scan of the diffraction efficiency with a 500-μm diaphragm.

the y-direction. However, the experimental two-dimensional scan might be strongly influenced by the shape of the crystal surfaces as the Bragg-condition is only fulfilled at the position of maximal diffraction efficiency. Furthermore, if the radius of equal intensity r_e is reduced in the simulations, the diffraction efficiency drops much faster along the z-axis.

Maximal diffraction efficiency

Only one free parameter is used to conduct the simulations shown in Fig. 4.26, Fig. 4.28, and Fig. 4.29: The radius of equal intensity r_e for the 400-nm hole. The radius for the 1000-nm hole is derived from this value. Besides this, literature values have been used for the material parameters. Even though the absolute values of the diffraction efficiency differ considerably between simulation and experiment, we expect that the model is able to predict the relative height of the different measurements.

Figure 4.16 shows that the maximal diffraction efficiency is $\eta = 5.5 \times 10^{-4}$ for a 1000-nm hole, $\eta = 5.7 \times 10^{-5}$ for a 500-nm hole, $\eta = 2.0 \times 10^{-5}$ for a 400-nm hole. Simulated diffraction efficiencies are found in Fig. 4.26 and a numerical simulation not shown here for a 500-nm hole: $\eta = 1.8 \times 10^{-2}$ for a 1000-nm hole, $\eta = 2.3 \times 10^{-3}$ for a 500-nm hole, $\eta = 1.5 \times 10^{-3}$ for a 400-nm hole. Thus, within the relatively large error, the dependence on the hole size of the simulated data is the same as in the experiment.

Figure 4.15 and Fig. 4.13 show that the diffraction efficiency is three

orders of magnitudes smaller for a 400-nm hole compared with that of the plane-wave case. The question arises which effects decrease the diffraction efficiency by such a large amount.

The first issue to discuss is the size of the readout-beam. The diffraction efficiency is calculated by dividing the diffracted light power by the power imping on the crystal. If light enters the crystal in regions which do not contribute significantly to the diffracted light, the diffraction efficiency is lowered, because this light contributes to the power impinging onto the crystal, but not to the light being diffracted. As we see in the two-dimensional scan in Fig. 4.20, the area of significant diffraction is much smaller than the crystal volume.

The amplitude of the signal wave decreases rapidly in the crystal, according to $|A_S| \propto \exp(-r\alpha/2)/r$. When this inhomogeneous light wave interferes with the relatively homogeneous plane wave the contrast of the interference pattern, i.e., the degree of modulation m_g, becomes inhomogeneous. Full contrast can only be reached in a small fraction of the crystal. We use Eq. (4.30) to calculate how this effect influences the overall diffraction efficiency. In Fig. 4.30 the diffraction efficiency is plotted versus the radius of equal intensity. For the bottom curve the hologram is truncated outside a $\mathrm{NA_h} = 2.0$ cone, thus exotic gratings are not considered. This curve shows a maximum at $r_e = 2\,\mathrm{mm}$, i.e., the degree of modulation is maximal in the center of the crystal. This is in accordance to the analysis in [83]. No maximum is found if the hologram is not truncated. This is, because the side lobes of the signal wave are much weaker than the central peak and for high r_e the side lobes contribute more to the diffraction than the central diffraction cone. Thus, the region of maximal contrast is far away enough from the hole for the exotic gratings for very high r_e only. This is the reason, why no maximum is found in the considered interval of r_e, if exotic gratings are taken into account.

The inhomogeneous degree of modulation and the crystal size are taken into account by our model. Thus, now we compare the maximal diffraction efficiency as it is predicted from the model with the experimental data, e.g., Fig. 4.17 and Fig. 4.26. We find a factor of 50 between the maximal diffraction efficiencies for the 400-nm hole. Several effects might explain these differences between simulation and experiment. Besides an incorrect radius of equal intensity r_e, reflection at the crystal surfaces, holographic scattering, and off-Bragg read-out because of non-planar crystal surfaces diminish the diffraction efficiency. These effects are the same as for the plane-wave case, where these effects account for a factor of about twelve.

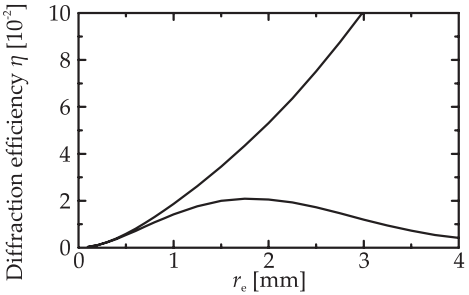

Figure 4.30: Calculated diffraction efficiency for different values of the radius of equal intensity r_e. For the bottom curve the hologram is truncated outside a $NA_h = 2.0$ cone.

Some other aspects might play a role for holography through a hole and do not for plane-wave holography: First, not all the phase-conjugated light emerging from the sub-wavelength hole might be collected by the microscope objective so that the measured η is just a fraction of the real diffraction efficiency. However, considering the diffraction patterns of circular apertures, for a NA $= 0.65$ microscope objective we do not expect this to play a significant role for hole diameters above $2r_h = 400\,\text{nm}$. Second, the transmission coefficient T_h of the hole in the gold film might be smaller than one. And third, by the compensation effect described before, the maximal space-charge amplitude would be diminished by a factor of $\max[t\exp(-t)] \approx 37\,\%$ and, accordingly, the maximal diffraction efficiency would be decreased, too [81].

In the center of our discussion in the previous sections is the diffraction efficiency η: The amount of diffracted power divided by the light power impinging onto the crystal. Thus, this value answers the question of how efficient the impinging light is used and thus might be an application relevant value. Furthermore, it is this magnitude which is at the heart of most discussions about volume holograms in the literature. However, there are certain aspects, which are to be kept in mind for an adequate interpretation of the diffraction efficiency: First, light is focused and the intensity is enhanced at the hole, even for very small η. A diffraction efficiency of $\eta = 3 \times 10^{-5}$ is measured for a 400-nm hole. Normalized to the area of the hole this corresponds to an intensity enhancement of more than 7000 in re-

spect to the reference intensity. Second, even if 100 % of the read-out light is diffracted, only a small fraction is focused onto the area of the hole, and the remaining light is reflected, because the focus is bigger than the hole. This fraction is an upper bound to the diffraction efficiency. A comparison with plane-wave values becomes meaningless.

The reconstructed spot

Figure 4.31 shows an image of the calculated phase-conjugated signal wave S^*. The 400-nm hole is supposed to be at the center of the image. To calculate the spot size, the model including the exotic gratings is used and Eq. 4.30 is evaluated. The reconstructed spot roughly fits to the original 400-nm hole. But the spot is not a smooth disc, but has a more complicated structure, which is due to the complicated grating pattern in the crystal.

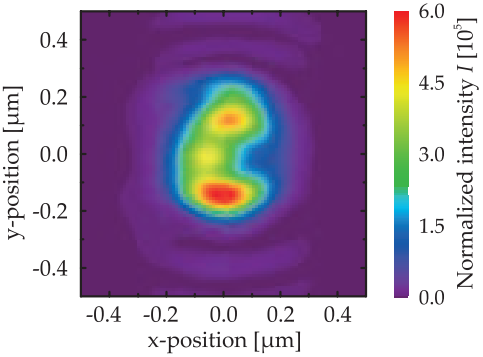

Figure 4.31: Simulated profile of the phase-conjugated signal wave, for a 400-nm hole. The intensity is normalized to the impinging read-out wave intensity.

4.4.4 Optimizing holography through a hole

Optimizing the diffraction efficiency

Assume that all experimental issues are solved: Perfectly planar crystal surfaces, which have an anti-reflection coating. Furthermore, holographic scattering shall be negligible, the compensation effect should not occur,

and all the diffracted light should be transmitted through the hole and shall be measured by the photodiode. This is the situation, where theoretical considerations should coincide with experimental data. Furthermore, we assume that the size of the read-out beam and the radius of equal intensity should be freely adjustable. We ask, what the performance of such an idealized system is.

The model presented in the last section is appropriate to explain the experimental data, as long as the diffraction efficiency is very small. But, if we optimize for far higher maximal diffraction efficiency, the assumption of the first-order Born approximation is violated: Depletion of the read-out light is no longer negligible and determines the optimal parameters. This is why we skip finding parameters for a maximal diffraction efficiency as given by our model. However, up to now, most model parameters are chosen based on the values used in the experiments. Many parameters, e.g., the crystal size and the hole diameter, are determined by practical reasons rather than optimal conditions. Therefore, we start with a $W_x = W_y = W_z = 1\,\mathrm{mm}$ sized crystal and a radius of equal intensity of $r_\mathrm{e} = 0.5\,\mathrm{mm}$ and calculate the diffraction efficiency for a sub-wavelength hole with a diameter of 40 nm. Even if the small wavelength of the light inside of the crystal is considered, this absolutely fulfills $r_\mathrm{h} \ll \lambda$. Hence, the modeled signal wave becomes an isotropic spherical wave.

Figure 4.32 shows the reconstructed spot for a 40-nm hole. The central region has a radius of the first dark ring of 120 nm in the x-direction and 90 nm in the y-direction. According to Eq. (4.37) this corresponds to a numerical aperture of $\mathrm{NA_h} = 2.2$ in the x-direction and $\mathrm{NA_h} = 3.0$ in the y-direction. For the y-direction, the numerical aperture is higher than the index-of-refraction of $n = 2.3$, but strong secondary maxima occur in the $\pm y$-direction. A similar effect happens in a telescope, where by blocking the central part of the circular aperture the focus size is reduced [12].

Varying the radius of equal intensity, a maximal diffraction efficiency of $\eta = 7.2 \times 10^{-3}$ is found at $r_\mathrm{e} = 0.6\,\mathrm{mm}$. By decreasing the crystal size to $W_z = 230\,\mu\mathrm{m}$ the diffraction efficiency increases up to 1.6 %. We can compare this to a diffraction limited spot with a numerical aperture of $\mathrm{NA} = 1$ for a wavelength of $\lambda_0 = 532\,\mathrm{nm}$: According to Fraunhofer diffraction about 1.4 % of the light power of a diffraction limited spot is within a radius of 20 nm. Thus, due to a higher numerical aperture, the transmitted light power already is slightly enhanced in our simulation. Further improvements can be made by scaling the hologram to a larger size. However, only 2.7 % of the light seen in Fig. 4.32 fall within the circle

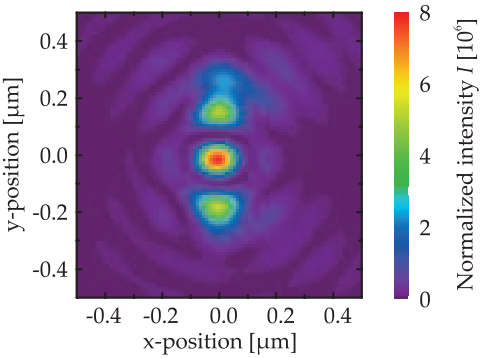

Figure 4.32: Simulated profile of the phase-conjugated signal wave, for a 40-nm hole. The intensity is normalized to the impinging read-out wave intensity.

of the hole. Thus even if 100 % of the incoming light would be diffracted by the hologram, we would measure a diffraction efficiency of just 2.7 %. Due to pump depletion of the read-out beam, this value is therefore an upper bound of the diffraction efficiency for a 40-nm hole.

Some optimizations are possible for iron-doped lithium niobate crystals. By oxidizing the crystal, the amplitude of the electric space-charge field ΔE_{SC} is enhanced and absorption is reduced [80]. As a drawback, the recording time is prolonged by oxidization, making stability issues even more important. Rotating the c-axis by 45° the average space-charge field ΔE_{SC} can be enhanced, as the grating vector becomes parallel to the c-axis of the crystal for signal wave vectors along the z-axis and thus in the center of the crystal.

Alternative recording materials

Alternative recording materials like photosensitive glasses [84–86] or photo-addressable polymers [87, 88] could improve the performance of the system. However, these materials have other drawbacks: Recording in photosensitve glasses is irreversible and requires a high-temperature development process and photo-adressable polymers are only available as films and not as thick bulk material, and these polymers show strong absorption. In isotropic materials no compensation effect and no depen-

dence on the grating orientation occurs. Materials with a smaller response time do not need an active stabilization, and all practical complications due to the stabilization system could be circumvented. Nevertheless, an optimal size and an optimization of the degree of modulation would still be needed.

Improvements of the model

The model proposed herein could be improved for more accurate predictions of the performance of a high-numerical-aperture system by holographic phase conjugation. First, a refined expression for the diffracted light transmitted through holes with diameters comparable to the wavelength would be useful. This expression could be extracted from transmission experiments or finite differences time domain numerical calculations. A further improvement would be a full vectorial instead of our pseudo-vectorial calculation. Further considerations could include the complicated time dependence of the grating build-up. Finally improvements, e.g., coupled wave equations, to go beyond the first-order approximation, would allow better determination of optimal parameters.

4.5 Summary

Phase-conjugation through a sub-wavelength hole in a metal film on top of iron-doped lithium niobate crystal is possible and leads to a nicely focused spot. The holograms recorded through a hole show some unique differences compared to those of the plane-wave case, especially a more complex temporal evolution of the diffraction efficiency and a more peculiar distribution of grating vectors.

The temporal evolution of the diffraction efficiency can be understood, if the crystal is not completely illuminated. Then, charges accumulate at the border of the illuminated area and a field compensating the bulk photovoltaic current builds up. Since this current is the major driving force for grating build up, the gratings are erased and the diffraction efficiency drops to lower values.

A model of a hologram recorded by a wave transmitted through a sub-wavelength hole and a plane wave is introduced. Besides material parameters which are taken from literature, there is mainly one free parameter: The relative intensity of the reference wave R and the signal wave S, ex-

pressed as a radius of equal intensity r_e. Diffraction from this hologram is described by a scalar first-order Born approximation. For a relatively small value of $r_e = 0.2\,\mathrm{mm}$ for a 400-nm hole, the radius r_e is calculated for other hole sizes, and the experimental data can be qualitatively well described: The angular selectivity curves, including the unexpected asymmetry, the razor-blade measurements and the two-dimensional scan, and the long term saturation value, when the hologram is read-out close to the hole. Additionally, within the error, the relative height of the maximal diffraction efficiency for three different hole sizes is predicted correctly by the simulation.

Rather unexpectedly, the experiments confirm that exotic gratings contribute significantly to the diffracted light: gratings recorded by beams having different polarizations, found close to the x-y-plane, and being phase-shifted to the interference pattern. Thus diffracted waves from a wide range of directions contribute to the reconstructed spot, resulting in a very high effective numerical aperture.

For phase conjugation through a 400-nm hole, the diffraction efficiency is experimentally found to be only $\eta \approx 3 \times 10^{-5}$. This is three orders of magnitudes smaller than that for the plane-wave case. The overall diffraction efficiency very sensitively depends on the radius of equal intensity r_e. We do not know these parameters very exactly. However, the order of magnitude of the diffraction efficiency is understandable, mainly due to two effects: The small average degree of modulation, because r_e is very small, and the size of the crystal is chosen non-optimal.

Several approaches to optimize for higher diffraction efficiencies can be found as the holograms are analyzed more closely. From simulations of holography through a 40-nm hole on a $1 \times 1 \times 0.23\,\mathrm{mm}^3$-sized crystal, a diffraction efficiency of 1.6 % is calculated. This is slightly larger than the fraction of light falling onto the hole by focusing with a NA $= 1$ microscope objective.

Compared to conventional focusing systems, holographic phase conjugation through a sub-wavelength hole on an iron-doped lithium niobate crystal has two potential advantages: first, an extremely high numerical aperture NA due to the high index-of-refraction and the possibility to record exotic, anisotropic gratings. And second, the method is not limited to single holes, but sophisticated patterns of sub-wavelength openings can be addressed with a very high NA. In contrast to conventional focusing, this capability is potentially available in a very high field of view.

Chapter 5

Summary

Though huge efforts have been made, only poor knowledge, whether theoretical or experimental, is available on the transmission characteristics of optical nanophotonic structures, in particular a single sub-wavelength hole in a real metal. However, it is known that the transmitted power becomes a tiny fraction of the impinging light, when the hole is very small compared with the wavelength. For many real-life applications far higher efficiencies of the light transmitted through a nano-aperture are needed. Ways to enhance the transmission are highly desirable. Thus, we are looking for methods, with which the transmission is higher than through the pure sub-wavelength hole. For comparison: by structuring the area surrounding the hole, an one-order-of-magnitude enhancement of the transmission efficiency has been reported. The scope of this work are two novel methods to enhance the transmission through a sub-wavelength hole. Both methods rely on the constructive interference of light waves impinging onto the hole right before transmitting it.

The first method is the external Fabry-Pérot-enhanced transmission. There, a partially transmitting mirror and the metal film with the sub-wavelength hole form a cavity. The resulting transmittance is enhanced by a factor of more than 20 by the additional mirror. Thus, the transmission is augmented more than what has been achieved by structures surrounding the sub-wavelength hole. The dependence of the enhancement and the finesse on the transmission coefficient of the input mirror can be excellently modeled by adapting the well-known formula for the Fabry-Pérot interferometer. The limiting finesse, which is achievable with the available system and mirrors, is about 105. From this analysis it is concluded, that with further optimization an enhancement of 100 is achievable.

The second method under investigation is holographic phase conjugation through a sub-wavelength hole in a gold film directly on top of an iron-doped lithium niobate crystal. Light being transmitted through the hole and a plane reference wave record a hologram. This hologram is read-out by the phase-conjugated reference wave. According to the holographic principle, the phase-conjugated signal wave, which is a back-propagating spherical wave, is reconstructed. Thus, light is focused onto the hole.

Experimentally, focusing is shown to work by recording a hologram through a 200-nm hole and subsequent removal of the gold film. The diffraction efficiency for a 400-nm hole is three orders of magnitudes smaller compared with that of a hologram recorded by two plane waves. A model is introduced to explain these experimental results: The signal wave is modeled by Kirchhoff diffraction. The position depending grating strength is calculated from material parameters from the literature. And diffraction from the hologram is simulated with the first-order Born approximation. Qualitatively the measured data are explained by this model. The small diffraction efficiency is mainly attributed to a non-optimal crystal size, a small degree of modulation of the interference pattern and other experimental issues. Unexpectedly, evidence is found that gratings anisotropically recorded close to the metal film contribute significantly to the diffraction. As simulations show, this results in a very high effective numerical aperture. Furthermore, the calculations indicate that due to the high numerical aperture an optimized holographic focusing system could indeed result in an intensity comparable or better than for a NA $= 1$ microscope objective. Especially for applications requiring a very high field of view, holographic phase-conjugation through a sub-wavelength hole might be superior to conventional focusing. However, considerable efforts would have to be undertaken to reach the theoretically predicted diffraction efficiencies.

Which of the methods to enhance the transmission of light through sub-wavelength structures, proposed in this work or in the literature, is preferable, depends on the application. However, in any case, external enhancement, which is the focus of this work, should be taken into account, when judging whether a nanophotonic application has the efficiencies needed for a real-life use.

Bibliography

[1] J. D. Joannopoulos, P. R. Villeneuve, and S. H. Fan, "Photonic crystals: Putting a new twist on light," Nature **386**, 143–149 (1997).

[2] J. B. Pendry, "Negative refraction makes a perfect lens," Phys. Rev. Lett. **85**, 3966–3969 (2000).

[3] R. A. Shelby, D. R. Smith, and S. Schultz, "Experimental verification of a negative index of refraction," Science **292**, 77–79 (2001).

[4] E. Betzig and J. K. Trautman, "Near-field optics - microscopy, spectroscopy, and surface modification beyond the diffraction limit," Science **257**, 189–195 (1992).

[5] W. L. Barnes, A. Dereux, and T. W. Ebbesen, "Surface plasmon subwavelength optics," Nature **424**, 824–830 (2003).

[6] E. Ozbay, "Plasmonics: Merging photonics and electronics at nanoscale dimensions," Science **311**, 189–193 (2006).

[7] H. A. Bethe, "Theory of diffraction by small holes," Phys. Rev. **66**, 163–182 (1944).

[8] T. W. Ebbesen, H. J. Lezec, H. F. Ghaemi, T. Thio, and P. A. Wolff, "Extraordinary optical transmission through sub-wavelength hole arrays," Nature **391**, 667–669 (1998).

[9] H. J. Lezec, A. Degiron, E. Devaux, R. A. Linke, L. Martin-Moreno, F. J. Garcia-Vidal, and T. W. Ebbesen, "Beaming light from a subwavelength aperture," Science **297**, 820–822 (2002).

[10] C. Genet and T. W. Ebbesen, "Light in tiny holes," Nature **445**, 39–46 (2007).

[11] J. Weiner, "The physics of light transmission through subwavelength apertures and aperture arrays," Rep. Prog. Phys. **72**, 064 401 (2009).

[12] M. Born and E. Wolf, *Principles of optics*, Springer series in optical sciences (Cambridge University Press, 1999), 7 edn.

[13] A. Roberts, "Electromagnetic theory of diffraction by a circular aperture in a thick, perfectly conducting screen," J. Opt. Soc. Am. A **4**, 1970–1983 (1987).

[14] L. Novotny and C. Hafner, "Light propagation in a cylindrical waveguide with a complex, metallic, dielectric function," Phys. Rev. E **50**, 4094–4106 (1994).

[15] R. Gordon and A. G. Brolo, "Increased cut-off wavelength for a subwavelength hole in a real metal," Opt. Exp. **13**, 1933–1938 (2005).

[16] P. B. Catrysse, H. Shin, and S. H. Fan, "Propagating modes in subwavelength cylindrical holes," J. Vac. Sci. Technol. **23**, 2675–2678 (2005).

[17] B. Sturman, E. Podivilov, and M. Gorkunov, "Eigenmodes for the problem of extraordinary light transmission through subwavelength holes," Europhys. Lett. **80**, 24 002 (2007).

[18] H. F. Ghaemi, T. Thio, D. E. Grupp, T. W. Ebbesen, and H. J. Lezec, "Surface plasmons enhance optical transmission through subwavelength holes," Phys. Rev. B **58**, 6779–6782 (1998).

[19] H. Raether, *Surface plasmons on smooth and rough surfaces and on gratings* (Springer, 1998).

[20] H. J. Lezec and T. Thio, "Diffracted evanescent wave model for enhanced and suppressed optical transmission through subwavelength hole arrays," Opt. Exp. **12**, 3629–3651 (2004).

[21] Y. Xie, A. R. Zakharian, J. V. Moloney, and M. Mansuripur, "Transmission of light through a periodic array of slits in a thick metallic film," Opt. Exp. **13**, 4485–4491 (2005).

[22] G. Gay, O. Alloschery, B. V. De Lesegno, C. O'Dwyer, J. Weiner, and H. J. Lezec, "The optical response of nanostructured surfaces and the composite diffracted evanescent wave model," Nat. Phys. **2**, 262–267 (2006).

[23] F. Kalkum, G. Gay, O. Alloschery, J. Weiner, H. J. Lezec, Y. Xie, and M. Mansuripur, "Surface-wave interferometry on single subwavelength slit-groove structures fabricated on gold films," Opt. Exp. **15**, 2613–2621 (2007).

[24] P. Lalanne and J. P. Hugonin, "Interaction between optical nano-objects at metallo-dielectric interfaces," Nat. Phys. **2**, 551–556 (2006).

[25] G. Leveque, O. J. F. Martin, and J. Weiner, "Transient behavior of surface plasmon polaritons scattered at a subwavelength groove," Phys. Rev. B **76**, 155 418 (2007).

[26] B. Ung and Y. L. Sheng, "Optical surface waves over metallo-dielectric nanostructures: Sommerfeld integrals revisited," Opt. Exp. **16**, 9073–9086 (2008).

[27] C. Obermüller and K. Karrai, "Far-field characterization of diffracting circular apertures," Appl. Phys. Lett. **67**, 3408–3410 (1995).

[28] A. Degiron, H. J. Lezec, N. Yamamoto, and T. W. Ebbesen, "Optical transmission properties of a single subwavelength aperture in a real metal," Opt. Commun. **239**, 61–66 (2004).

[29] J. Prikulis, P. Hanarp, L. Olofsson, D. Sutherland, and M. Kall, "Optical spectroscopy of nanometric holes in thin gold films," Nano Lett. **4**, 1003–1007 (2004).

[30] L. Yin, V. K. Vlasko-Vlasov, A. Rydh, J. Pearson, U. Welp, S. H. Chang, S. K. Gray, G. C. Schatz, D. B. Brown, and C. W. Kimball, "Surface plasmons at single nanoholes in Au films," Appl. Phys. Lett. **85**, 467–469 (2004).

[31] T. Thio, K. M. Pellerin, R. A. Linke, H. J. Lezec, and T. W. Ebbesen, "Enhanced light transmission through a single subwavelength aperture," Opt. Lett. **26**, 1972–1974 (2001).

[32] P. D. Flammer, I. C. Schick, R. T. Collins, and R. E. Hollingsworth, "Interference and resonant cavity effects explain enhanced transmission through subwavelength apertures in thin metal films," Opt. Exp. **15**, 7984–7993 (2007).

[33] T. Ishi, J. Fujikata, K. Makita, T. Baba, and K. Ohashi, "Si nano-photodiode with a surface plasmon antenna," Jpn. J. Appl. Phys. 2 **44**, L364–L366 (2005).

[34] C. Liu, V. Kamaev, and Z. V. Vardeny, "Efficiency enhancement of an organic light-emitting diode with a cathode forming two-dimensional periodic hole array," Appl. Phys. Lett. **86**, 143 501 (2005).

[35] M. M. Alkaisi, R. J. Blaikie, S. J. McNab, R. Cheung, and D. R. S. Cumming, "Sub-diffraction-limited patterning using evanescent near-field optical lithography," Appl. Phys. Lett. **75**, 3560–3562 (1999).

[36] X. G. Luo and T. Ishihara, "Sub-100-nm photolithography based on plasmon resonance," Jpn. J. Appl. Phys. 1 **43**, 4017–4021 (2004).

[37] W. Srituravanich, N. Fang, C. Sun, Q. Luo, and X. Zhang, "Plasmonic nanolithography," Nano. Lett. **4**, 1085–1088 (2004).

[38] G. Hernandez, *Fabry-Pérot Interferometers* (Cambridge University Press, 1988).

[39] M. Vaughan and J. M. Vaughan, *The Fabry-Pérot interferometer* (Institute of Physics Publishing, 1989).

[40] J. J. Olivero and R. L. Longbothum, "Empirical fits to the Voigt line width: A brief review," J. Quant. Spectrosc. Ra. **17**, 233 – 236 (1977).

[41] E. E. Whiting, "An empirical approximation to the Voigt profile," J. Quant. Spectrosc. Ra. **8**, 1379–1384 (1968).

[42] P. B. Johnson and R. W. Christy, "Optical-constants of noble-metals," Phys. Rev. B **6**, 4370–4379 (1972).

[43] J. M. Bennett, J. L. Stanford, and E. J. Ashley, "Optical constants of silver sulfide tarnish films," J. Opt. Soc. Am. **60**, 224–231 (1970).

[44] R. O. Carter, "The effect of metal optical constants on far-infrared and mid-infrared reflection-absorption," Spectrochim. Acta, Part A **47**, 551–561 (1991).

[45] E. A. M. Baker and B. Walker, "Fabry-Pérot interferometers for use at submillimetre wavelengths," J. Phys. E **15**, 25–32 (1982).

[46] J. A. Ma, B. Catanzaro, J. E. Ford, Y. Fainman, and S. H. Lee, "Photorefractive holographic lenses and applications for dynamic focusing and dynamic image shifting," J. Opt. Soc. Am. A **11**, 2471–2480 (1994).

[47] W. H. Liu and D. Psaltis, "Pixel size limit in holographic memories," Opt. Lett. **24**, 1340–1342 (1999).

[48] B. L. Volodin, B. Kippelen, K. Meerholz, B. Javidi, and N. Peyghambarian, "A polymeric optical pattern recognition system for security verification," Nature **383**, 58–60 (1996).

[49] Z. Yaqoob, D. Psaltis, M. S. Feld, and C. Yang, "Optical phase conjugation for turbidity suppression in biological samples," Nat. Phot. **2**, 110–115 (2008).

[50] G. Barbastathis, M. Levene, and D. Psaltis, "Shift multiplexing with spherical reference waves," Appl. Opt. **35**, 2403–2417 (1996).

[51] B. Vohnsen and S. I. Bozhevolnyi, "Holographic approach to phase conjugation of optical near fields," J. Opt. Soc. Am. A **14**, 1491–1499 (1997).

[52] G. Lerosey, J. De Rosny, A. Tourin, and M. Fink, "Focusing beyond the diffraction limit with far-field time reversal," Science **315**, 1120–1122 (2007).

[53] K. Buse, "Light-induced charge transport processes in photorefractive crystals I: Models and experimental methods," Appl. Phys. B **64**, 273–291 (1997).

[54] H. Kogelnik, "Coupled wave theory for thick hologram gratings," Bell Syst. Tech. J. **48**, 2909–2947 (1969).

[55] K. Buse, "Light-induced charge transport processes in photorefractive crystals II: Materials," Appl. Phys. B **64**, 391–407 (1997).

[56] H. Kurz, E. Krätzig, W. Keune, H. Engelmann, U. Gonser, B. Dischler, and A. Räuber, "Photorefractive centers in $LiNbO_3$, studied by optical, Mössbauer, and EPR-methods," Appl. Phys. **12**, 355–368 (1977).

[57] N. V. Kukhtarev, V. B. Markov, S. G. Odoulov, V. L. Soskin, and V. L. Vinetskii, "Holographic storage in electrooptic crystals," Ferroelectrics **22**, 949–960, 961–964 (1979).

[58] G. Montemezzani and M. Zgonik, *Photorefractive materials and their applications 1*, Springer series in optical sciences (Springer, 2006), chap. Space-charge driven holograms in anisotropic media.

[59] P. Bernasconi, I. Biaggio, M. Zgonik, and P. Günter, "Anisotropy of the electron and hole drift mobility in $KNbO_3$ and $BaTiO_3$," Phys. Rev. Lett. **78**, 106–109 (1997).

[60] A. M. Glass, D. von der Linde, and T. J. Negran, "High-voltage bulk photovoltaic effect and photorefractive process in $LiNbO_3$," Appl. Phys. Lett. **25**, 233–235 (1974).

[61] B. I. Sturman and V. M. Fridkin, *The photovoltaic and photorefractive effects in noncentrosymmetric materials* (Gordon and Breach science publishers, 1992).

[62] P. Jullien, P. Mathey, P. Lompre, A. Novikov, and S. Odoulov, "Coupling of ordinary and extraordinary waves in iron-doped $BaTiO_3$ by a grating recorded by spatially oscillating photovoltaic currents," J. Opt. Soc. Am. B **13**, 2615–2621 (1996).

[63] M. Jazbinsek and M. Zgonik, "Material tensor parameters of $LiNbO_3$ relevant for electro- and elasto-optics," Appl. Phys. B **74**, 407–414 (2002).

[64] P. Günter and M. Zgonik, "Clamped-unclamped electro-optic coefficient dilemma in photorefractive phenomena," Opt. Lett. **16**, 1826–1828 (1991).

[65] E. Serrano, V. Lopez, M. Carrascosa, and F. Agullo-Lopez, "Steady-state photorefractive gratings in $LiNbO_3$ for strong light-modulation depths," IEEE J. Quantum. Elect. **30**, 875–880 (1994).

[66] E. Serrano, V. Lopez, M. Carrascosa, and F. Agullo-Lopez, "Recording and erasure kinetics in photorefractive materials at large modulation depths," J. Opt. Soc. Am. B **11**, 670–675 (1994).

[67] G. Montemezzani and M. Zgonik, "Light diffraction at mixed phase and aborption gratings in anisotropic media for arbitrary geometries," Phys. Rev. E **55**, 1035–1047 (1997).

[68] D. Gabor, "A new microscopic principle," Nature **161**, 777–778 (1948).

[69] S. Q. Tao, B. Wang, G. W. Burr, and J. B. Chen, "Diffraction efficiency of volume gratings with finite size: corrected analytical solution," J. Mod. Opt. **51**, 1115–1122 (2004).

[70] O. J. F. Martin and N. B. Piller, "Electromagnetic scattering in polarizable backgrounds," Phys. Rev. E **58**, 3909–3915 (1998).

[71] B. Gombkoto, P. Koppa, A. Suto, and E. Lorincz, "Computer simulation of reflective volume gratings holographic data storage," J. Opt. Soc. Am. A **24**, 2075–2081 (2007).

[72] F. Kalkum, "Fast numerical simulation of diffraction from large volume holograms," accepted by J. Opt. Soc. Am. A (2009).

[73] G. Barbastathis and D. Psaltis, *Holographic data storage*, Springer series in optical sciences (Springer, 2000), chap. Volume holographic multiplexing methods.

[74] A. M. Lopez, M. P. Arroyo, and M. Quintanilla, "Some polarization effects in holographic volume gratings," J. Opt. A **1**, 378–385 (1999).

[75] R. Magnusson and T. K. Gaylord, "Laser scattering induced holograms in lithium niobate," Appl. Opt. **13**, 1545–1548 (1974).

[76] D. L. Staebler and J. J. Amodei, "Coupled wave analysis of holographic strorage in $LiNbO_3$," J. Appl. Phys **43**, 1042–1049 (1972).

[77] R. A. Rupp and F. W. Drees, "Light-induced scattering in photorefractive crystals," Appl. Phys. B **39**, 223–229 (1986).

[78] S. Odoulov, K. Belabaev, and I. Kiseleva, "Degenerate stimulated parametric scattering in $LiTaO_3$," Opt. Lett. **10**, 31–33 (1985).

[79] S. Breer, K. Buse, K. Peithmann, H. Vogt, and E. Krätzig, "Stabilized recording and thermal fixing of holograms in photorefractive lithium niobate crystals," Rev. Sci. Instrum. **69** (1998).

[80] K. Peithmann, A. Wiebrock, and K. Buse, "Photorefractive properties of highly doped lithium niobate crystals in the visible and near-infrared," Appl. Phys. B **68**, 777–784 (1999).

[81] F. Kalkum, K. Peithmann, and K. Buse, "Dynamics of holographic recording with focused beams in iron-doped lithium niobate crystals," Opt. Exp. **17**, 1321–1329 (2009).

[82] S. Schwalenberg, "Computation of the intensities of parametric holographic scattering patterns in photorefractive crystals," Phys. Rev. E **71**, 066 608 (2005).

[83] F. Kalkum, S. Broch, T. Brands, and K. Buse, "Holographic phase conjugation through a sub-wavelength hole," Appl. Phys. B **95**, 637–645 (2009).

[84] G. J. Steckman, W. Liu, R. Platz, D. Schroeder, C. Moser, and F. Havermeyer, "Volume holographic grating wavelength stabilized laser diodes," IEEE J. Sel. Top. Quant. **13**, 672–678 (2007).

[85] B. L. Volodin, S. V. Dolgy, E. D. Melnik, E. Downs, J. Shaw, and V. S. Ban, "Wavelength stabilization and spectrum narrowing of high-power multimode laser diodes and arrays by use of volume Bragg gratings," Opt. Lett. **29**, 1891–1893 (2004).

[86] T. Y. Chung, A. Rapaport, V. Smirnov, L. B. Glebov, M. C. Richardson, and M. Bass, "Solid-state laser spectral narrowing using a volumetric photothermal refractive Bragg grating cavity mirror," Opt. Lett. **31**, 229–231 (2006).

[87] S. J. Zilker, T. Bieringer, D. Haarer, R. S. Stein, J. W. van Egmond, and S. G. Kostromine, "Holographic data storage in amorphous polymers," Adv. Mater. **10**, 855–859 (1998).

[88] R. Hagen and T. Bieringer, "Photoaddressable Polymers for optical data storage," Adv. Mater. **13**, 1805–1810 (2001).

Acknowledgements

First of all, my deep and sincere gratitude goes to Karsten Buse. He welcomed me in his group to write my diploma thesis and later offered to do my Ph.D. studies there. His profound knowledge on holography, his dedication to a high level of quality control, and his interest in the well-being of those who work with him are an example. I also greatly thank Manfred Fiebig for agreeing to co-assess my thesis.

During my studies, I had the opportunity to work in two international research groups. I deeply thank John Weiner from the Paul-Sabatier university in Toulouse and George Barbasthatis from the Massachusetts Institute of Technology in Boston for the opportunities to work with them. My gratitude also goes to the members of their groups.

Several people accompanied me for some time: The diploma students Thorsten Brands and Sebastian Broch, the master student Mathieu Gentile, and the Bachelor student Manuel Peter. Their work greatly enriched this thesis and their contribution is invaluable. In addition, several students contributed by doing internships: Katharina Brands, Nils Hoffmann, Henning Brammer, and Felix von Cube. I enjoyed working with them very much and profited a lot.

I owe Konrad Peithmann deep thanks for sharing his knowledge and for his help. In addition, several people supported me working on my thesis and I want to express my sincere appreciation of their contribution. Some of these people are: Dirk Apitz, Tobias Beckmann, Ingo Breunig, Lena Jentjens, and Tobias Jungk. Furthermore, my thanks go to all former and current members of the Heinrich-Hertz research group.

Michael Kösters and Sebastian Broch proof-read my thesis. Rosita Sowade and Hendrik Steigerwald read parts of it. I express my great gratitude for their efforts.

My great appreciation also goes to the workshops, which fabricated many parts of the experimental setup, to Hildegard Hodde, who made the gold films, and to Angelika Sehrbrock, who operates the focused-ion-beam apparatus at the research center caesar.

The scholarship of the Deutsche Telekom Stiftung is greatly appreciated, not only because of the financial support but also for all the events from which I personally benefited. Thanks also go to the Bonn-Cologne graduate school for physics and astronomy. Furthermore, I greatly appreciate the financial support of the Deutsche Forschungsgemeinschaft (FG FOR 557) and the Deutsche Telekom AG.